Correspondence to:
Y. Irie,
yoshiya.irie.290@s.kyushu-u.ac.jp

Nonmonotonic Postdeglacial Relative Sea Level Changes at the Aftermath of Marinoan (635 Ma) Snowball Earth Meltdown

Yoshiya Irie[1] , Masao Nakada[2], Jun'ichi Okuno[3], and Huiming Bao[4,5]

[1]Department of Earth and Planetary Sciences, Graduate School of Science, Kyushu University, Fukuoka, Japan, [2]Department of Earth and Planetary Sciences, Faculty of Science, Kyushu University, Fukuoka, Japan, [3]National Institute of Polar Research, Tachikawa, Japan, [4]Institute of Geochemistry, Chinese Academy of Sciences, Guiyang, China, [5]Department of Geology and Geophysics, Louisiana State University, Baton Rouge, LA, USA

Abstract Marinoan snowball Earth offers us a set of sedimentary and geochemical records for exploring glacial isostatic adjustment (GIA) associated with one of the most severe glaciations in Earth history. An accurate prediction of GIA-based relative sea level (RSL) change associated with a snowball Earth meltdown will help to explore sedimentary records for RSL changes and to place independent constraints on mantle viscosity and on the durations of syndeglaciation (T_d) and cap carbonate deposition. Here we mainly examine postdeglacial RSL change characterized by an RSL drop and a resumed transgression inferred from the cap dolostones on the continental shelf in south China. Such a nonmonotonic RSL behavior may be a diagnostic GIA signal for the Marinoan deglaciation resulting from a significantly longer postdeglacial GIA response than that for the last deglaciation. A postdeglacial RSL drop followed by transgression in south China, which is significantly affected by Earth's rotation, is predicted over the continental shelf for models with $T_d \leq 20$ kyr and a deep mantle viscosity of ~5 × 10²² Pa s regardless of the upper mantle viscosity. The inferred GIA model also explains the postdeglacial RSL changes such as sedimentary-inferred RSL drops on the continental shelf in northwestern Canada and California at low-latitude regions insignificantly affected by Earth's rotation. Furthermore, the good match between the predicted and observed RSL changes in south China suggests an approximate duration of ~50 kyr for the Marinoan ^{17}O depletion event, an atmospheric event linked to the post-Marinoan drawdown of CO_2 and the concurrent rise of O_2.

1. Introduction

The Earth system, including its hydrosphere, atmosphere, and biosphere, must have experienced dramatic transformations to a new steady state after a large perturbation such as a snowball Earth global glaciation. One such Earth system response is the large magnitude relative sea level (RSL) change that occurred in association with a snowball episode (Hoffman, 2011). The Marinoan snowball Earth, which ended at ~635 Ma, offers us the best sedimentary and geochemical records for studying the RSL history of Earth system response to such a large perturbation and its accompanied changes in the atmosphere and biosphere.

RSL changes in the aftermath of Marinoan snowball meltdown have been inferred from the deposition of cap dolostones (Hoffman et al., 2007), and a 1- to 1.5-km eustatic sea level (ESL) rise for the Marinoan deglaciation was estimated from the Otavi Group sediment of Namibia (Hoffman, 2011). Hoffman and Macdonald (2010) examined the depositional environments of cap dolostones for the Congo and Kalahari cratons in Namibia and inferred a sequence of transgression, regression, and transgression during the melting phase, referred to as the syndeglacial phase here (see Figure 1b). They proposed that both transgression phases are due to ice sheet melting and that the regression interrupting the transgressive cap dolostone sequence is caused by the loss of gravitational attraction between ice sheet and seawater, as analogous to the RSL change in Greenland from the last deglaciation in the Late Pleistocene (Clark, 1976). The regression is inferred from the presence of deeper water turbidites at the base of the lower-slope sections associated with the Otavi bank (Hoffman et al., 2007) and from the interpretation of the formation of sheet cracks near the base of the cap dolostones on the margins of the Congo and Kalahari cratons

(Hoffman & Macdonald, 2010). Zhou et al. (2010) inferred a sequence of transgression, regression, and transgression based on the stratigraphic studies of cap dolostones in south China. They proposed that the first transgression is due to a rapid ice sheet melting in the syndeglacial phase. However, they interpreted the karst-like dissolution features at the top of the cap dolostones as a brief disruption or hiatus in carbonate sedimentation, possibly a brief time window of RSL drop when the rate of isostatic rebound exceeded that of the general transgression. The subsequent growth of crystal fans of barite, or in some cases perhaps aragonite, occurring in the inner surface of cavities or outer surface of boulders or breccia in some topographically high areas marks a second transgression at a time after the complete glacial meltdown, referred to as the postdeglacial phase here.

Predictions for RSL changes due to glacial isostatic adjustment (GIA) associated with a snowball Earth would be crucial in interpreting the sedimentary-inferred RSL changes such as those in Congo/Kalahari and south China cratons. Liu and Peltier (2013) examined the RSL changes due to snowball glaciation based on the model with a 570-Ma continental configuration, a flat land surface and ocean bottom, and a ~1,000-m ESL change. They estimated the RSL drop along continental coastlines at equilibrium state during the snowball period and concluded that the predicted elevations of the land surface above the ocean surface are broadly consistent with the estimate of the depth difference between a carbonate platform and its lower slope from the Otavi Group sediment of Namibia.

Creveling and Mitrovica (2014) were the first to examine the spatial and temporal patterns of GIA-based RSL changes due to Marinoan snowball deglaciation. They adopted a 635-Ma paleogeographic reconstruction and topography consistent with mean values in modern topography. Their results show that (i) the predicted RSL changes exhibit significant geographic variability, including a syndeglacial RSL drop or stillstand at some sites and (ii) that sea level continues to rise in the postdeglacial phase in some areas, and thus, the timescale for transgressive cap dolostone deposition needs not to be confined to the syndeglacial phase. It is instructive that the variability in their sea level histories encompasses the range of variability in sedimentary-inferred RSL changes for specific geologic sites. However, their results did not include nonmonotonic RSL behavior in the postdeglacial phase characterized by an RSL drop and a resumed transgression, such as that inferred in south China. We note that such a nonmonotonic RSL behavior is not expected in the postdeglacial phase for the last deglaciation (e.g., Tushingham & Peltier, 1991). The postdeglacial phase of the Last Glacial Maximum (LGM) that peaked at ~21 kyr ago was of duration ~10 kyr (e.g., Lambeck et al., 2014). That is, nonmonotonic RSL behavior arises from a significantly longer postdeglacial GIA response than that for the last deglaciation and may be a diagnostic GIA signal for Marinoan snowball deglaciation.

Here we evaluate RSL changes associated with Marinoan snowball deglaciation by considering the effects of time-dependent shoreline migration and ocean bathymetry (Lambeck et al., 2003; Milne et al., 1999) and their uncertainties, as well as Earth's rotation (Milne & Mitrovica, 1996; Mitrovica et al., 2005). We must also consider paleotopography describing the location of paleoshorelines and paleowater depths when we discuss the RSL change inferred from sedimentary records. Our focus here will be to examine postdeglacial RSL change characterized by an RSL drop and a resumed transgression such as those in south China, and this history may also be sensitive to mantle viscosity structure. Moreover, the results may help to constrain the rate of an expectedly drastic evolution of the Earth system in the aftermath of a snowball state, for example, the duration of the syndeglaciation, the duration of cap dolostone deposition, and the recovery rate of the biosphere. All are closely linked to a global rate of weathering, organic burial, changing ocean chemistry, the rise of atmospheric O_2, and fall of atmospheric CO_2 concentrations (Bao et al., 2008; Cao & Bao, 2013). Thus, our modeling study can offer an independent test on the timing and duration of the Marinoan ^{17}O depletion (MOSD) event as recorded in basal Ediacaran sedimentary rocks worldwide.

The paper is organized as follows. In section 2, we describe the viscosity and ice models, as well as models for continental distribution, topography, and ocean bathymetry. In section 3, we examine the syndeglacial and postdeglacial RSL changes by considering the impacts of coastline geometry, syndeglacial duration and mantle viscosity on the syndeglacial and postdeglacial RSL drops. In section 4, we compare sedimentary-inferred and predicted RSL changes and try to establish some constraints on the syndeglacial duration, mantle viscosity, and the duration of the MOSD. The results obtained in this study are summarized in section 5.

2. Model Descriptions

The numerical method adopted here follows Nakada et al. (2016). Briefly, solving the sea level equation for the GIA processes (Farrell & Clark, 1976) requires an input of viscoelastic Earth structure, geography/topography, and ice sheet models. We use the seismological Preliminary Reference Earth Model (Dziewonski & Anderson, 1981) for density and elastic constants. We adopt two types of rheological model. One is a simple three-layer viscosity model characterized by elastic lithospheric thickness (H), upper mantle viscosity (η_{um}), and lower mantle viscosity (η_{lm}). The adopted values for H, η_{um}, and η_{lm} are $H = 65$, 100, and 200 km, $\eta_{um} = (2, 4, 7) \times 10^{20}$ Pa s, and $\eta_{lm} = (5, 10, 50) \times 10^{21}$ Pa s. Lambeck et al. (2014) indicated a typical value of 2×10^{20} Pa s for the oceanic upper mantle viscosity from analyses of far-field ocean islands and continental margin RSL data largely influenced by isostatic response due to the oceanic upper mantle viscosity. Lambeck et al. (2017) have also inferred an average continental upper mantle viscosity of $(3.5-7.5) \times 10^{20}$ Pa s and effective lithospheric thickness of $(85-120)$ km from GIA-related geological and geophysical data in the glaciated region for the North American Late Wisconsin ice sheet. The values of $H = 65$ km and $\eta_{um} = 4 \times 10^{20}$ Pa s are the same as those inferred from the observed RSL changes due to the melting of British and Scandinavian ice sheets (Lambeck & Johnston, 1998). The upper mantle viscosity of 4×10^{20} Pa s may be an average value for the above references (e.g., Lambeck et al., 2017; Nakada & Lambeck, 1991). The lower mantle viscosity of 5×10^{21} Pa s may be a lower bound as inferred from the Holocene sea level observations in the Australian region (Nakada & Lambeck, 1989) and joint inversion using GIA and convection data sets (Mitrovica & Forte, 2004). The values of $\eta_{lm} = 5 \times 10^{22}$ Pa s are consistent with recent estimates from GIA studies based on far-field sea level data by Lambeck et al. (2014) and from LGM sea levels at Barbados and Bonaparte Gulf and the rate of change of degree-two zonal harmonic of Earth's geopotential due to GIA process by Nakada et al. (2016). More recent analyses using GIA data sets due to the last deglaciation yield a deep mantle viscosity of $\sim 10^{23}$ Pa s (Lau et al., 2016; Nakada et al., 2018; Nakada & Okuno, 2016). We therefore adopt a two-layer lower mantle viscosity model defined by $\eta_{670,1191} = 5 \times 10^{21}$ Pa s (viscosity for 670- to 1,191-km depth) and $\eta_{1191,2891} = 5 \times 10^{22}$ Pa s (viscosity for 1,191- to 2,891-km depth). The values for H and η_{um} are the same as those for the simple three-layer viscosity model. Creveling and Mitrovica (2014) adopted lower mantle viscosities of 5×10^{21} and 2×10^{22} Pa s and evaluated the RSL change relative to a reference time of up to 100 kyr after the complete melt. The highest lower mantle viscosity adopted here is 5×10^{22} Pa s, and we therefore evaluate the RSL change relative to sea level predicted at a reference time of 1 Myr after the complete melt. We ran tests by calculating RSL over longer periods than 1 Myr and did not see significant changes in the predicted RSL changes. From the above, we see that these parameters for our Earth models are deduced for the last Ice Age. Since the Earth has been cooling and mantle viscosity is temperature-dependent, the parameters for lithospheric thickness and mantle viscosities should be changing with time too. In section 4.1, we will investigate the effects of this change in average temperature between the Marinoan and the present.

We explain geography/topography models adopted here. The continental distribution, topography of the land, and ocean bathymetry are uncertain yet important in evaluating the RSL changes at 635 Ma. Here we adopt the continental distribution of the 635 Ma from Li et al. (2013; see Figure 2a) and the ratio of ocean area over Earth's surface area is 0.73. The assumed topography at the reference time (initial topography prior to Marinoan snowball glaciation) is based on mean values in modern topography and is shown in Figure 1a. This topography model is the same as that used by Creveling and Mitrovica (2014). The continental margin areas shallower than $\sim -1,000$-m depth (Figure 1a) are main depositional places of cap dolostones for sedimentary-inferred RSL changes. Particularly, the postdeglacial RSL changes examined in this study are inferred from cap dolostones for the continental shelf areas. We therefore examine the impacts of the coastline geometry and ocean bathymetry and their uncertainties on RSL changes by considering cases with a gulf or a peninsula. A paleotopography $TP(x, t)$ at a time t and position x, which is required in discussing sedimentary-inferred RSL change, is related to the $RSL(x, t)$ by $TP(x, t) = T(x) + I(x, t) - RSL(x, t)$ where $T(x)$ and $I(x, t)$ are the topography at the reference time and the grounded ice thickness, respectively (e.g., Lambeck, 1997). Our studied GIA-based RSL changes occurred in a total period of less than 1 Myr, from the syndeglacial to postdeglacial phases. The mean topography will change with time, but we think that those long-term changes probably introduce uncertainties less than what the different coastline geometry models would in our modeling study.
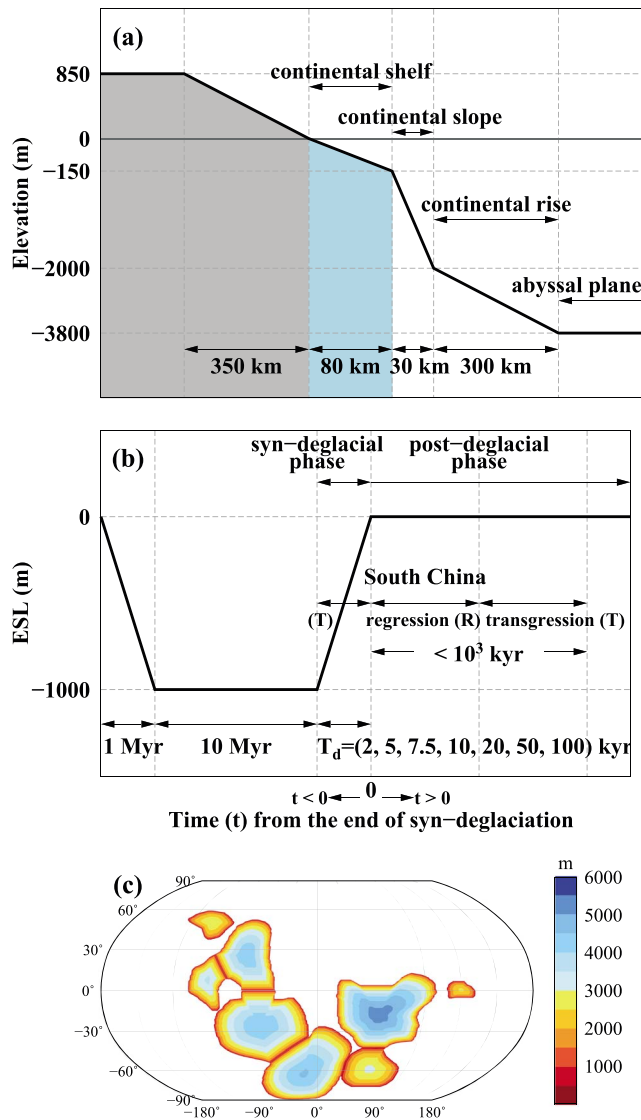
Figure 1. (a) Schematic figure for the cross section of the assumed topography of the solid Earth surface at the reference time (initial topography prior to Marinoan snowball glaciation). (b) Schematic eustatic sea level (ESL) histories illustrating syndeglacial phase with a duration T_d and postdeglacial phase ($t > 0$), and the approximate time of the transgressions (T) and the interrupting regression (R) in south China. The duration of the regression and transgression in the postdeglacial phase is based on the reference time adopted in this study (1 Myr). (c) Grounded ice thickness distribution at the maximum glaciation.

Next, we explain the ice model (see Figures 1b and 1c). We assume that ice covers all continents during glacial maximum and the total ESL change is 1,000 m, as assumed by Creveling and Mitrovica (2014). From the conservation of ice and water mass for the assumed ocean area (73% of the Earth's surface area), we get a mean ice thickness of about 3,000 m. ESL linearly decreases within a period of 1 Myr followed by a constant value of −1,000 m for a period of 10 Myr reflecting a full snowball phase (Figure 1b). In the syndeglacial phase, we assume a globally synchronous melting for all ice sheets, which is one of the cases considered by Creveling and Mitrovica (2014), and ESL linearly increases starting at the onset of syndeglacial phase. The duration of syndeglaciation is represented by T_d. The value of T_d is treated as variable. Rapid deglaciation with a duration of 2–10 kyr has been inferred from ice sheet dynamics (Hyde et al., 2000) and by analogy with Quaternary deglaciation (Hoffman et al., 2007). Such a rapid deglaciation is also consistent with an estimate of $T_d \sim 6$ kyr based on a paleohydraulic analysis of wave ripples and tidal laminae of the Elatina Formation, Australia (Myrow et al., 2018). Paleomagnetic polarity reversals from the analyses of cap dolostones suggest a deposition duration of longer than 100 kyr (Hoffman et al., 2007; Kilner et al., 2005; Trindade et al., 2003), although this inference is not necessarily equal to the syndeglacial duration. On the other hand, Creveling et al. (2016) suggested that the cap carbonate platform of the Noonday Formation in SE California records crustal rebound (1–100 kyr) for the whole syndeglacial phase. Here, we adopt $T_d = 2, 5, 7.5, 10, 20, 50$, and 100 kyr to examine its effects on RSL change. The distribution of ice thickness is constructed based on the method by Lambeck (1993) in which the maximum ice thickness at the center of ice sheet is proportional to the square root of the distance of the ice margin from the center (Paterson, 1969). The grounded ice thickness distribution at the maximum glaciation is shown in Figure 1c. The grounded ice at this phase covers all continents and continental shelves and also continental slope areas shallower than ~−1,000-m depth (Figure 1a) as inferred from ESL value shown in Figure 1b. That is, these continental margin areas would be main depositional places for cap dolostones in the syndeglacial and/or postdeglacial phases. The impacts of their uncertainties on RSL changes are examined based on a coastline geometry model with a gulf or a peninsula. Here the glaciated area at an arbitrary time is estimated based on an assumption that the glaciated area decreases in proportion to the ice volume derived from the ESL component (Nakada et al., 2016).

Finally, our model carries an assumption in calculating Earth's rotation and rotational feedback on sea level change. Changes in Earth's rotational axis due to GIA-based Earth deformation perturb the centrifugal potential causing the redistribution of water load, which also causes an additional solid Earth deformation (Milne & Mitrovica, 1996; Mitrovica et al., 2005). The 635-Ma paleogeographic reconstruction adopted here (Li et al., 2013) assumes that the geomagnetic pole approximates the position of the geographic pole. Here we assume that the position of the rotation axis at the onset of the snowball glaciation was coincident with the geographic pole for the 635-Ma paleogeographic reconstruction (Figure 1c).

3. Results

In this section, we report the syndeglacial and postdeglacial RSL changes by considering the impacts of coastline geometry, syndeglacial duration, and mantle viscosity on the syndeglacial and postdeglacial RSL drops. It would be useful to mention sea level components for GIA-based RSL change before discussing the results. The RSL change is contributed by ESL (ice volume equivalent sea level) component (RSL_esl, see

Figure 1b), sea level component due to the gravitational attraction between ice sheet and seawater loads (RSL_{att}), and the viscoelastic response of the Earth to ice sheet (RSL_{ice}) and seawater (RSL_{water}) loads, that is, $RSL = RSL_{esl} + RSL_{att} + RSL_{ice} + RSL_{water}$ (e.g., Farrell & Clark, 1976; Nakada & Lambeck, 1987). In this study, the term RSL_{water} includes the contribution to sea level change from Earth's rotation. The terms RSL_{esl} and RSL_{att} are zero in the postdeglacial phase, and the RSL_{att} term was proposed by Hoffman and Macdonald (2010) to explain the regression interrupting the transgressive cap dolostone sequence in Namibia.

This section is organized as follows. In section 3.1, we show the syndeglacial RSL drop by considering the impact of coastline geometry on the syndeglacial RSL change. In section 3.2, we demonstrate the postdeglacial RSL change by focusing on cases with an RSL drop followed by a transgression in the postdeglacial phase, a pattern inferred from sedimentary records such as those in south China. In section 3.2.1, we show that RSL change in south China is affected significantly by Earth's rotation and that RSL changes at low-latitude regions are driven largely by the collapse of the peripheral bulge. In section 3.2.2, we examine the sensitivities of RSL change in south China to mantle viscosity, syndeglacial duration, and changes in the location of south China. In section 3.2.3, we examine the sensitivities of RSL changes at low-latitude regions to coastline geometry, mantle viscosity, and syndeglacial duration.

3.1. Syndeglacial RSL Change

In the syndeglacial phase, the continental slope would be a main depositional place for cap dolostones. Here we examine the GIA-based syndeglacial RSL change for the continental slope by considering an episode of regression interrupting a cap dolostone transgressive sequence inferred from the stratigraphic studies of cap dolostones in Namibia. Creveling and Mitrovica (2014) analyzed the syndeglacial RSL drop in detail, and they indicated that the RSL drop interrupting a cap dolostone transgressive sequence is only one of the GIA-based RSL patterns and it can be attributed to one of the three processes (or their combination) of local melting, crustal uplift in regions of significant ice loss, and an extended syndeglacial phase of duration ~50 kyr or greater, with all scenarios of RSL drop to be confined to the syndeglacial phase. Adopting a viscosity model with $H = 65$ km, $\eta_{um} = 4 \times 10^{20}$ Pa s, $\eta_{lm} = 10^{22}$ Pa s and a syndeglacial duration of 20 kyr ($T_d = 20$ kyr), our model predicts an RSL drop followed by transgression in the syndeglacial phase for shaded blue and gray regions (Figure 2). The shaded blue regions (Figures 2d and 2e) signify ocean areas as defined by the paleotopography (i.e., site below sea level at a time when RSL drop occurs), and gray regions signify land areas (i.e., site above sea level at a time when RSL drop occurs). In the following we use "ocean" to refer to points with negative paleotopography values and "land" to refer to points with positive paleotopography values. Figures 2b–2e show contour maps of the syndeglacial RSL drop (red color) for Regions A and C–E in Figure 2a. The contour line for the initial topography is shown by the black line. The RSL drops for Regions A and C occur within land areas, and those in ocean areas are predicted to occur at the inner part of the gulf in Region D and at the channel in Region E.

We explore the syndeglacial RSL changes at Sites C1 to C3 in Figure 3a. Sites C1 and C2 are located on the coastline and outer edge of the continental shelf at the initial topography, respectively. Site C3, which is located on the continental slope, corresponds to the site in Namibia where Hoffman and Macdonald (2010) inferred an episode of regression interrupting a cap dolostone transgressive sequence. Figure 3b shows RSL changes at Sites C1 to C3. The RSL changes predicted for ocean sites are shown by solid lines, and those for land sites are shown by dotted lines. The RSL at Site C3 in the ocean gradually rises from −20 to 0 kyr, and that for Site C1 on land shows an RSL drop with a magnitude of ~30 m from −20 to −17 kyr followed by an RSL rise from −17 to 0 kyr.

We now explore the impact of coastline geometry on the predicted syndeglacial RSL drop. Within Region C we observe a fall in RSL for land-based sites (Figures 3a and 3b), but the inner part of the gulf in Region D clearly shows an RSL drop within the ocean (Figure 2d). This is consistent with the results by Creveling and Mitrovica (2014) that regions of significant ice loss are subject to large land rebound and are characterized by the syndeglacial RSL drop. We also consider the Coastline Geometry Models M1 with a gulf of width and length (4°, 4°) for Region C (Figure 3c) and M2 (Figure 3e) characterized by a peninsula of width and length (4°, 4°). The peninsula in M2 is located on the continental shelf (see 0-m contour line for the topography in Figure 3e). These coastline geometry models reflect uncertainties of the paleogeography and have analogies
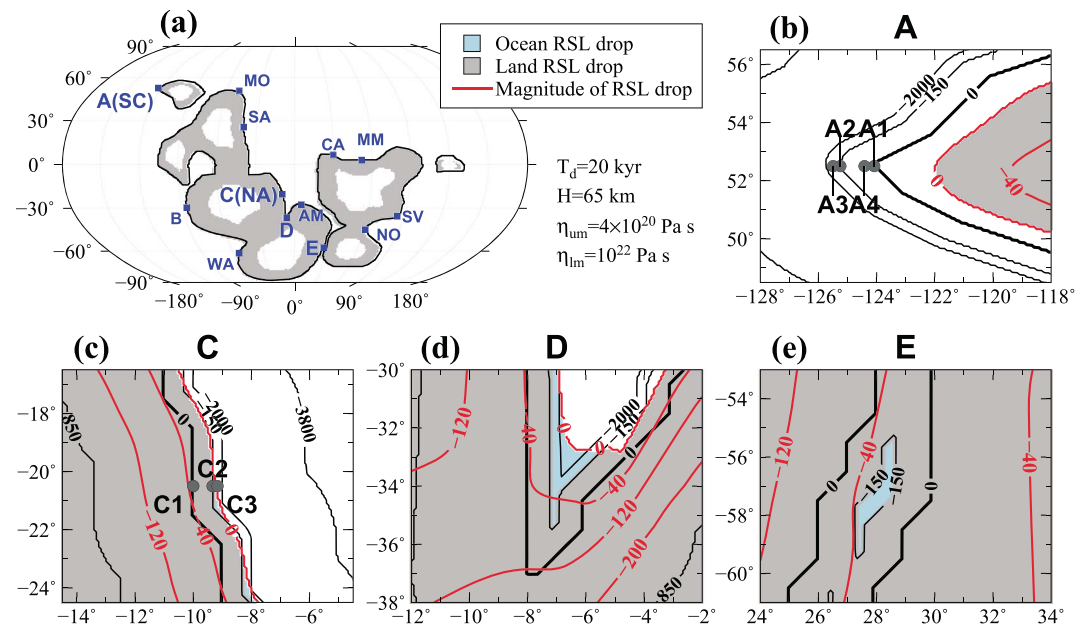
Figure 2. (a) Spatial distribution for relative sea level (RSL) drop in the syndeglacial phase based on the model with the Coastline Geometry Model M0, $T_d = 20$ kyr, $H = 65$ km, $\eta_{um} = 4 \times 10^{20}$, and $\eta_{lm} = 10^{22}$ Pa s. Regions lying below sea level that experience a fall in RSL are shaded blue (see panels d and e), and regions lying above sea level that experience a fall in RSL are gray. Labels refer to the following locations: SC = south China; WA = West Africa; MO = Zavkhan Terrane of southwestern Mongolia; SA = South Australia; NA = Namibia; AM = southern Amazon; CA = California; MM = Mackenzie Mountains, northwestern Canada; SV = Svalbard; NO = East Finnmark of Norway. (b–e) The contour maps of the RSL drop (red color) in the syndeglacial phase for Regions A and C–E. The contour line for the initial topography is shown by the black line.

in present-day coastline geometries. For example, the gulf for M1 is like Bay of Biscay and the peninsular for M2 is like Grand Banks of Newfoundland.

Our Coastline Geometry Model M1 predicts a syndeglacial RSL drop within the continental slope (Figure 3c). This is because the crustal uplift (RSL fall) at the continental slope site for M1 is significantly larger than that for M0, and consequently, the magnitude of RSL fall due to the loss of gravitational attraction between ice and ocean loads (RSL_{att} term) and local crustal uplift (RSL_{ice} term) exceeds the ESL rise (RSL_{esl} term). The predicted syndeglacial RSL drop is consistent with a regression in the syndeglacial phase inferred from the cap dolostones on the lower-slope sections of the Congo and Kalahari cratons (Hoffman & Macdonald, 2010). We next consider the Coastline Geometry Model M2 (Figures 3e and 3f). An RSL drop within the ocean is not predicted for the region around the tip of the peninsula (Site g6), but it is predicted for the region around the base of the peninsula with a coastline geometry similar to a gulf (Site g3). Although we do not show the results, the magnitude of the RSL drop increases as the size of the gulf and ratio of the length to width of the gulf is increased. However, our numerical experiments for such coastline geometry models do not predict a syndeglacial RSL drop within the continental shelf because the continental shelf lies above sea level until the late stage of the syndeglacial phase. This remains true if the syndeglacial RSL drop is attributed to a rapid localized melting event, as indicated by Creveling and Mitrovica (2014).

3.2. Postdeglacial RSL Change
3.2.1. Impacts of Earth's Rotation and Collapse of Peripheral Bulge on RSL Change
In the postdeglacial phase, continental shelf becomes a main depositional setting for cap dolostones. Here we examine the postdeglacial RSL change in continental shelf areas by focusing on cases with an RSL drop followed by a transgression in the postdeglacial phase, a pattern inferred from sedimentary records such as those in south China (Zhou et al., 2010). Figures 4a–4c show the spatial and temporal variations of postdeglacial RSL changes (black contour lines) based on a model with $T_d = 2$ kyr, $H = 65$ km, $\eta_{um} = 4 \times 10^{20}$ Pa s, $\eta_{lm} = 5 \times 10^{22}$ Pas and Coastline Geometry Model M0. We explain these spatial variations by considering
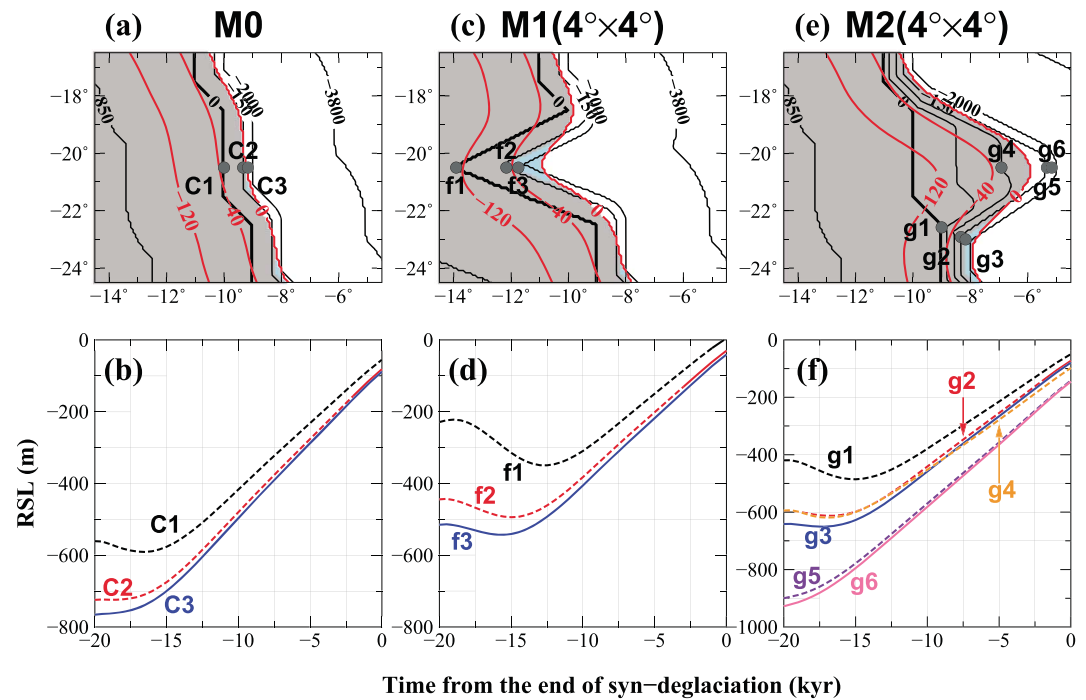
Figure 3. (a) Contour map of the relative sea level (RSL) drop (red color) in the syndeglacial phase for Regions C based on the Coastline Geometry Model M0. Regions lying below sea level that experience a fall in RSL are shaded blue (see panels c and e), and regions lying above sea level that experience a fall in RSL are gray. The contour line for the initial topography is shown by the black line. (b) RSL changes at Sites C1–C3 shown in panel (a) based on the model with $T_d = 20$ kyr, $H = 65$ km, $\eta_{um} = 4 \times 10^{20}$ and $\eta_{lm} = 10^{22}$ Pa s. The RSL change predicted at ocean site for the paleotopography is shown by the solid line, and that at land site is shown by the dotted line. (c and d) As in panels (a) and (b) except for M1. (e and f) As in panels (a) and (b) except for M2. Sites C1(f1, g1), C2(f2, g2, g5), and C3(f3, g3, g6) are located on the coastline, outer edge of the continental shelf, and continental slope at the initial topography, respectively.

GIA response to surface load distribution. Ice and water loads are assumed to be 0 before the glaciation. In the glacial phase, ice load is positive in the continent and water load is negative in the ocean. Both the ice loading and the water unloading cause downward crustal movement in the continent and upward crustal movement in the ocean. Here we use "peripheral bulge" to refer to the upward displacement in the ocean due to both loads. In the postdeglacial RSL changes shown in Figures 4a–4c, continental regions exhibit RSL fall due to the crustal rebound, and their peripheral areas exhibit RSL rise due mainly to the crustal subsidence (collapse of the peripheral bulge). Red lines show the boundary between the RSL fall region and the RSL rise one (referred to as hinge line here). Continental margins are almost equivalent with the hinge lines at $t = 0$ kyr. Over time, the hinge lines move outward or seaward as a whole and long-wavelength RSL components become dominant (e.g., see RSL changes at $t = 50$ kyr in Figure 4c). These temporal and spatial variations are related to the time-dependent behavior of the peripheral bulge when the adopted viscosity model is characterized by $\eta_{lm} \gg \eta_{um}$ (e.g., Cathles, 1975) and may be crucial in interpreting the postdeglacial RSL change for some continental shelf areas, a depositional location for cap dolostones. Creveling and Mitrovica (2014) discussed the postdeglacial RSL change but did not describe sedimentary-inferred nonmonotonic postdeglacial RSL behavior such as that inferred in south China. Here we explore the nonmonotonic RSL behavior by considering the impact of the collapse of peripheral bulge, Earth's rotation, coastline geometry and the paleogeography on the GIA-based RSL change.

Evaluating a GIA-based RSL change needs to take Earth's rotation into consideration (Milne & Mitrovica, 1996). Figure 4d shows the difference between the RSL changes at $t = 50$ kyr for rotating and nonrotating Earth models. Although we do not show the results, the peak value for an adopted ESL history model (Figure 1b) depends insignificantly on the ice thickness distribution, geography, and topography models but is proportional to the peak ESL amplitude and is affected by the presence of a sawtooth ESL history.
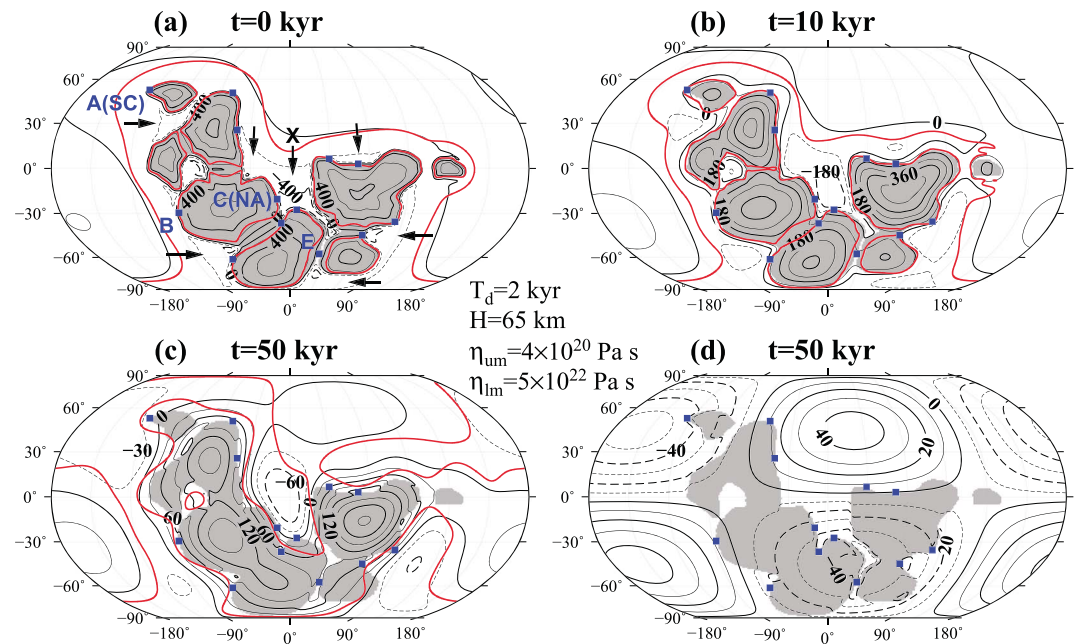
Figure 4. (a–c) Relative sea level (RSL) changes at $t = 0$, 10, and 50 kyr and (d) rotational component at $t = 50$ kyr based on the model with the Coastline Geometry Model M0, $T_d = 2$ kyr, $H = 65$ km, $\eta_{um} = 4 \times 10^{20}$, and $\eta_{lm} = 5 \times 10^{22}$ Pa s. Contour intervals for panels (a)–(d), solid black line for positive value and dashed black one for the negative, are 200, 90, 30, and 10 m, respectively. Red line shows the boundary between the RSL fall region and RSL rise one (referred to as hinge line here). Labels for panel (a) are the same as those for Figure 1a. The gray regions represent and areas for the initial topography.

The impact of Earth's rotation on the RSL change is dominated by a degree 2 and order 1 harmonic signal. The RSL at $t = 50$ kyr for Region A is ~−30 m (Figure 4c), and its rotational component is ~−40 m (Figure 4d), implying that the magnitude of the rotational component is significantly larger than the other components associated with ice sheet and seawater loads (~10 m). At Region E, located close to the opposite side of Region A, the RSL change at $t = 50$ kyr is positive and its rotational component is negative, implying that its RSL change is dominated by ice unloading and meltwater loading effects. That is, the Earth's rotation has significant impacts on the RSL change at midlatitude and isolated region, like south China.

Next, we examine the spatial distribution of nonmonotonic RSL behavior by considering the time-dependent hinge-line movement. Figures 5a–5d show the transition time from postdeglacial RSL fall to rise for four lower mantle viscosity models. We only show the transition that occurs on land or continental shelf for $t \leq 80$ kyr. The transition area increases with increasing lower mantle viscosity, and the general pattern for $\eta_{lm} = 5 \times 10^{22}$ Pa s is similar to that for a two-layer lower mantle viscosity model with $\eta_{670,1191} = 5 \times 10^{21}$ and $\eta_{1191,2891} = 5 \times 10^{22}$ Pa s. Figures 5e–5g show the hinge lines at $t = 0$, 10, 20, 50, and 70 kyr for Regions L–N (Figure 5c) based on the model with $\eta_{lm} = 5 \times 10^{22}$ Pa s. We first examine the overall relationship between RSL change and hinge line movement by considering typical spatial patterns of hinge-line movement predicted for Regions M and N. Figure 6a illustrates the relationship between RSL change and outward migration of hinge point for a period from 0 to 30 kyr based on the RSL change for the transect shown in Figure 5f. The hinge points at $t = 0$ and 30 kyr (X_0 and X_{30}) divide the RSL change into three types: RSL changes in Regions I, IIa, and III. RSL change in Region I, landward side for the hinge points from 0 to 30 kyr, is characterized by an RSL fall from 0 to 30 kyr. RSL change in Region IIa, seaward side for X_0 and landward side for X_{30}, is characterized by an RSL rise followed by an RSL fall. RSL change in Region III, seaward side for the hinge points at $t = 0$ and 30 kyr, is characterized by an RSL rise from 0 to 30 kyr. Figure 6b illustrates the RSL change for the transect shown in Figure 5g. RSL patterns in Regions I and III are the same as those for the outward migration of hinge point. However, RSL change in Region IIb, landward side for X_0 and seaward side for X_{30}, is characterized by an RSL drop followed by an RSL rise.
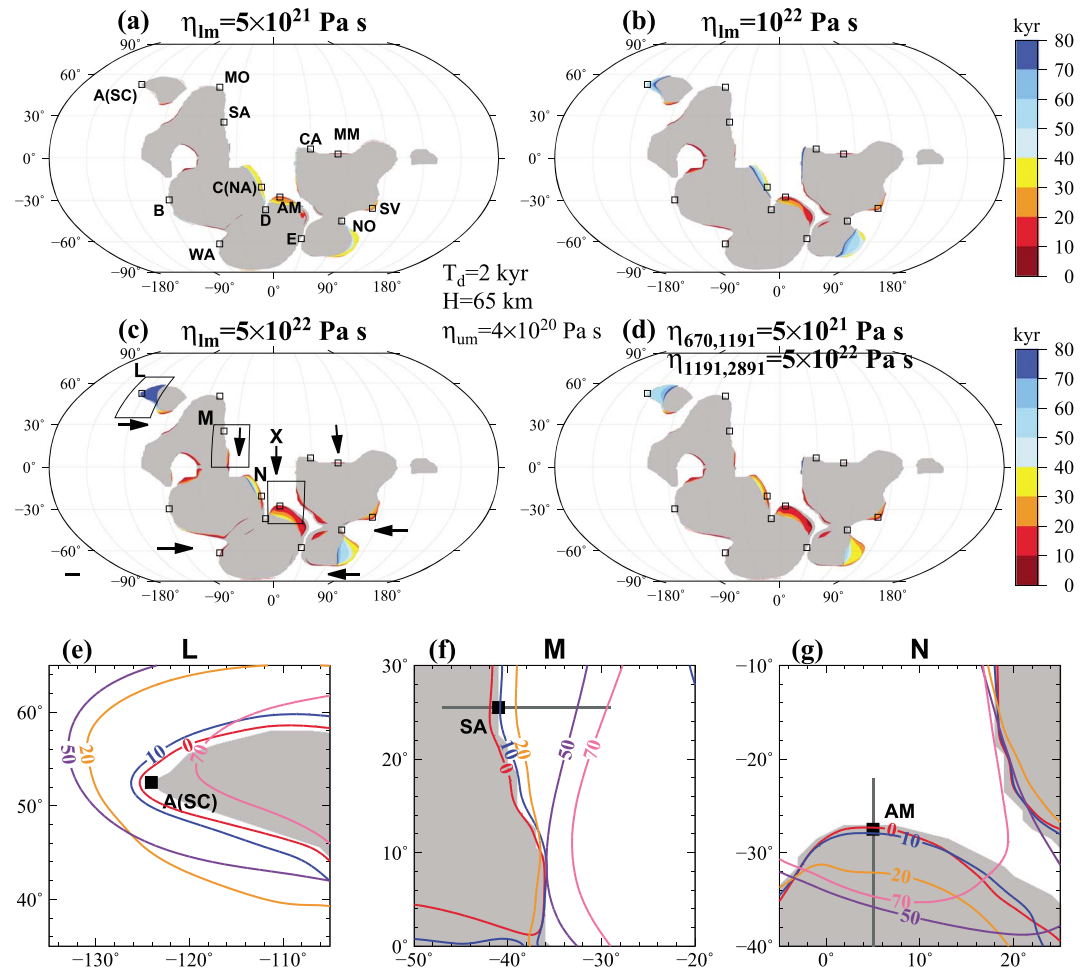
Figure 5. (a–d) The transition time from postdeglacial relative sea level fall to rise based on the Coastline Geometry Model M0, $T_d = 2$ kyr, $H = 65$ km, and $\eta_{um} = 4 \times 10^{20}$ Pa s. (a–c) The transition time for simple three-layer viscosity models with $\eta_{lm} = (5, 10, 50) \times 10^{21}$ Pa s and (d) the transition time for a two-layer lower mantle viscosity model with $\eta_{670,1191} = 5 \times 10^{21}$ and $\eta_{1191,2891} = 5 \times 10^{22}$ Pa s. Labels for panel (a) are the same as those for Figure 1a. (e–g) The hinge lines at $t = 0, 10, 20, 50,$ and 70 kyr for Regions L–N in panel (c) based on the model with $\eta_{lm} = 5 \times 10^{22}$ Pa s. The gray regions represent land areas for the initial topography.

We next consider the postdeglacial RSL change in Regions L, M, and N (Figures 5e–5g). The hinge line for Region L (south China), which is affected significantly by Earth's rotation (Figure 4d), migrates outward for $t \leq 50$ kyr and migrates inward for $t > 50$ kyr. Therefore, the RSL change at Site A, landward site of the hinge line for $t \leq 50$ kyr and seaward site for $t > 50$ kyr, shows an RSL fall for $t \leq 50$ kyr and RSL rise for $t > 50$ kyr. We discuss the postdeglacial RSL change in south China in more detail below (section 3.2.2). However, the postdeglacial RSL changes in Regions M and N have a negligible RSL contribution from Earth's rotation compared with south China (Figure 4d) and the postdeglacial RSL changes are significantly affected by time-dependent behavior of peripheral bulge. The hinge lines for the northern part of Region M show a continuous (monotonic) outward migration with the collapse of peripheral bulge, indicating a monotonic postdeglacial RSL fall on the landward side of the hinge line at $t = 0$ kyr and an RSL rise followed by an RSL fall on the seaward side (see Figure 6a). The hinge lines over the southern portion show an inward migration until ~20 kyr and then migrate outward, indicating a nonmonotonic RSL behavior characterized by an RSL drop for $t < 20$ kyr and a transgression for $t > 20$ kyr. The hinge lines for Region N show inward migration over a duration longer than 20 kyr (see Figure 6b). We can explore the mechanism for the nonmonotonic hinge-line movement by considering the impact of the adopted paleogeography model on the RSL change. Region N faces a relatively small ocean surrounded by continents ("X" in Figures 4a and 5c
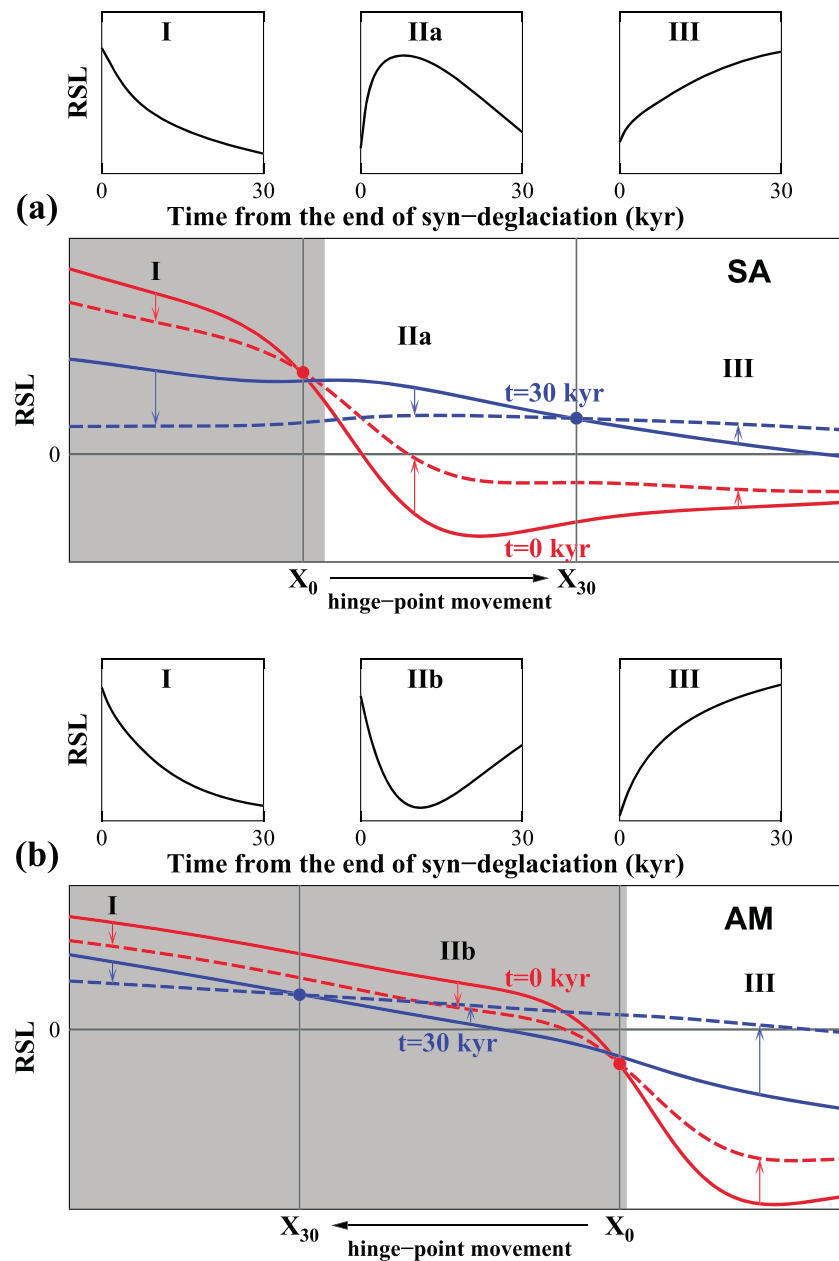
Figure 6. (a and b) Schematic illustrations of the relationship between relative sea level (RSL) change and hinge-point movement based on the RSL change for the transect (dark gray line) shown in Figures 5f and 5g. RSL changes at $t = 0$ and 30 kyr are shown by red and blue solid lines, respectively, and RSL changes at $t = 1$ and 35 kyr are shown by red and blue dashed lines, respectively. Note that the difference between solid and dotted lines is enlarged in order to emphasize the hinge points. The hinge points at $t = 0$ and 30 kyr (X_0 and X_{30}) divide the RSL change into three types: RSL changes in Regions I, IIa, and III for panel (a) and RSL changes in Regions I, IIb, and III for panel (b). The gray regions represent land areas for the initial topography.

referred to as ocean "X" here). The inward migration of the hinge line is primarily related to the subsidence of the ocean "X" due to ice unloading and meltwater loading effects as inferred from RSL changes predicted for the ocean "X" (Figures 4b and 4c). That is, the GIA response with a spatial scale of ocean "X" is probably a main cause for the nonmonotonic hinge-line movement for Regions N. This is true for other regions showing nonmonotonic RSL behavior, which face a small ocean surrounded by continents such as the ocean "X" or oceans (gulfs) indicated by arrows in Figure 5c (see also RSL changes in Figure 4b for these regions). We discuss the postdeglacial RSL changes for these regions in section 3.2.3 in more detail.
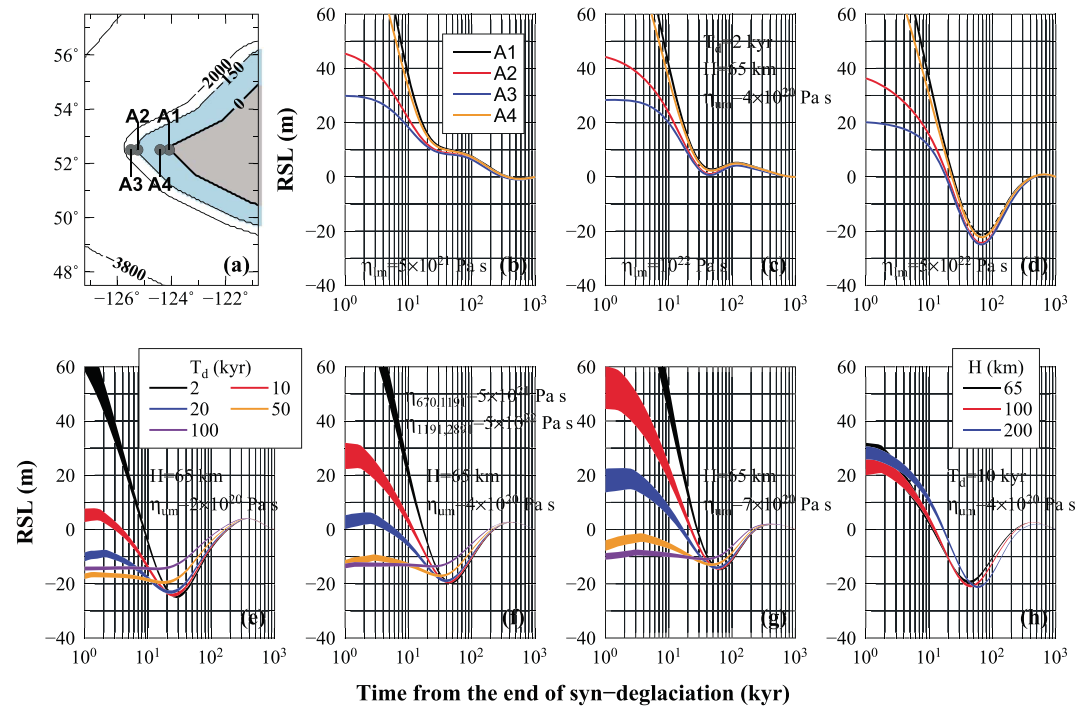
Figure 7. (a) An enlarged map for Region A. The shaded blue region represents the continental shelf for the initial topography, and the gray regions represent land areas. The contour line for the initial topography is shown by the black line. (b–d) Relative sea level (RSL) changes at Sites A1–A4 based on the models with $T_d = 2$ kyr, $H = 65$ km, $\eta_{um} = 4 \times 10^{20}$ Pa s, and $\eta_{lm} = (5, 10, 50) \times 10^{21}$ Pa s. The RSL change predicted at ocean site for the paleotopography is shown by the solid line, and that at land site is shown by the dotted line. (e–h) RSL changes for the region between Sites A1 and A4 based on the model with $\eta_{670,1191} = 5 \times 10^{21}$ and $\eta_{1191,2891} = 5 \times 10^{22}$ Pa s. (e–g) RSL changes for $T_d = (2, 10, 20, 50, 100)$ kyr, $H = 65$ km, and $\eta_{um} = (2, 4, 7) \times 10^{20}$ Pa s and (h) RSL changes for $T_d = 10$ kyr, $H = (65, 100, 200)$ km and $\eta_{um} = 4 \times 10^{20}$ Pa s. The coastline geometry model is M0.

3.2.2. Postdeglacial RSL Change in South China

We discuss the postdeglacial RSL change in south China. The following results are consistent with those derived from the hinge-line movement shown in Figure 5. Figure 7a shows an enlarged map for Region A based on the Coastline Geometry Model M0. Sites A1 and A2 are located on the coastline and outer edge of the continental shelf in the case of the initial topography, respectively. A postdeglacial transgression is not predicted for the viscosity model with $\eta_{lm} = 5 \times 10^{21}$ Pa s (Figure 7b) and is not clear for the model with $\eta_{lm} = 10^{22}$ Pa s (Figure 7c; see also Figures 5a and 5b). However, the viscosity model with $\eta_{lm} = 5 \times 10^{22}$ Pa s predicts an RSL drop followed by transgression in the postdeglacial phase over the continental shelf area between Sites A1 and A2 (Figure 7d). The RSL change at Site A4 is nearly identical to that for Site A1. Site A4 lies below sea level in the postdeglacial phase (denoted by a solid line), but Site A1 lies above sea level from 30 to 200 kyr (denoted by a dotted line). That is, the region between Sites A1 and A4 undergoes subaerial exposure at the regression-transgression transition. In this region, cap dolostones may undergo karstic dissolution, which is consistent with observed karst-like dissolution features at the top of the cap dolostones in south China. Zhou et al. (2010) interpreted these as requiring a brief disruption or hiatus in carbonate sedimentation, possibly reflecting a brief time window of an RSL drop.

We next consider a two-layer lower mantle viscosity model with $\eta_{670,1191} = 5 \times 10^{21}$ and $\eta_{1191,2891} = 5 \times 10^{22}$ Pa s (Figures 7e–7h). Figures 7e–7g show the predicted RSL changes between Sites A1 and A4 for each T_d value, and those for each H value are shown in Figure 7h. The thickness of the lines in Figures 7e–7h changes with time because the difference between the RSL changes at Sites A1 and A4 decreases with time. The two-layer lower mantle viscosity model with $\eta_{um} = 4 \times 10^{20}$ Pa s predicts an RSL drop followed by transgression (black line in Figure 7f), as is also predicted for the model with $\eta_{lm} = 5 \times 10^{22}$ and $\eta_{um} = 4 \times 10^{20}$ Pa s (Figure 7d). These results indicate that an RSL drop followed
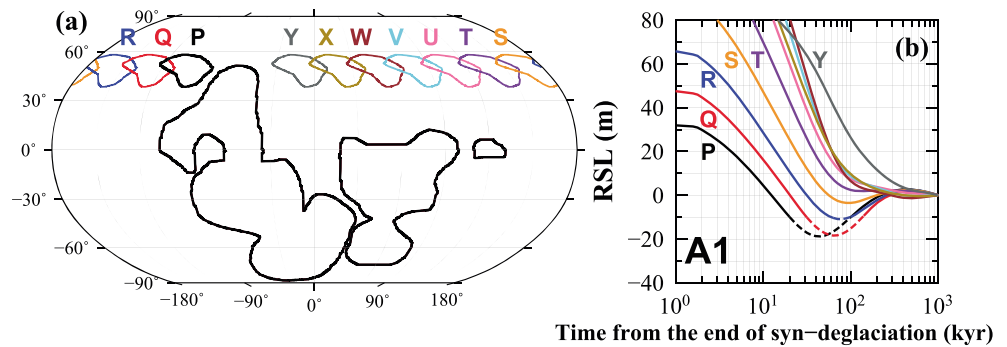
Figure 8. Illustrations to show the effects of paleogeography on relative sea level (RSL) change in south China based on the model with $T_d = 10$ kyr, $H = 65$ km, $\eta_{um} = 4 \times 10^{20}$, $\eta_{670,1191} = 5 \times 10^{21}$ and $\eta_{1191,2891} = 5 \times 10^{22}$ Pa s. (a) Ten different locations of south China denoted by "P" to "Y" obtained by taking the displacement in longitude direction of 30° to 270° relative to the original location of south China (location "P"). (b) The RSL changes at Site A1 for locations "P" to "Y" in panel (a). The RSL change predicted at ocean site for the paleotopography is shown by the solid line, and that at land site is shown by the dotted line.

by transgression in the postdeglacial phase is robust when we adopt a viscosity of ~5×10^{22} Pa s for the deep mantle. We also consider the effects of the lithospheric thickness (H), upper mantle viscosity (η_{um}), and syndeglacial duration (T_d) on postdeglacial RSL change. The general feature of the RSL change for $H = 100$ and 200 km is similar to that for $H = 65$ km (Figure 7h). Furthermore, the postdeglacial RSL changes for this region have the same sensitivities to syndeglacial duration, and a distinct RSL drop is predicted for the models with $T_d \leq 20$ kyr regardless of the upper mantle viscosity (Figures 7e–7g).

The exact paleogeography of south China or Yangtze Block at ~635 Ma has uncertainties (e.g., Hoffman & Li, 2009; Li et al., 2013). We therefore examine the sensitivity of the predicted RSL change at Site A1 to changes in the location of south China (Figure 8a). The 10 different locations of south China denoted by "P" to "Y" in Figure 8a are obtained by shifting the block in longitude by 30° to 270° relative to the original location of south China (location "P"), respectively. With increasing displacement in the longitude direction, the onset time of the second RSL rise increases and the magnitude of the second transgression decreases (Figure 8b). A second transgression is not predicted at locations "T" to "Y." This exercise shows that one must take into account uncertainties of the paleogeography when discussing the observationally inferred postdeglacial RSL change in south China. Conversely, it may be possible to put some constraints on the paleogeography from the observationally inferred RSL change.

3.2.3. Postdeglacial RSL Change at Low-Latitude Regions

In this section, we discuss the postdeglacial RSL changes for Regions B and C (Figure 4a) based on a model with $T_d = 2$ kyr, $H = 65$ km, $\eta_{um} = 4 \times 10^{20}$ Pa s, $\eta_{lm} = 5 \times 10^{22}$ Pa s and Coastline Geometry Models M0 and M2 (Figures 9 and 10). The discussion for Region B applies to other monotonic hinge-line movement regions and that for C applies to other nonmonotonic ones. The difference between the RSL changes for Regions B and C is attributed to the subsidence of the ocean "X" due to the ice sheet unloading and meltwater loading. We therefore examine the postdeglacial RSL change by decomposing the RSL change into ice (RSL_{ice}) and water (RSL_{water}) loading components, that is, $RSL = RSL_{ice} + RSL_{water}$. The terms RSL_{esl} and RSL_{att} are 0 in the postdeglacial phase. The term RSL_{ice} represents the variation in sea level associated with the loading and unloading of the ice sheets. The term RSL_{water} represents the contribution to sea level change caused by the seawater unloading and meltwater loading.

Figures 9a–9g show the hinge lines at $t = 0, 10, 20, 50,$ and 70 kyr, RSL_{ice} and RSL_{water} terms and RSL change for Region B based on the Coastline Geometry Model M0. The RSL changes for this region bear similar RSL patterns as shown in Figure 6a. The height of the peripheral bulge relative to the initial topography is approximately given by the negative value of predicted RSL change shown in Figure 9d, and the maximum height at $t = 0$ kyr is ~200 m around −91°E. Those for RSL_{ice} and RSL_{water} terms are ~120 and ~70 m, respectively (Figures 9b and 9c). We next examine the RSL change by considering the RSL_{ice} and RSL_{water} terms shown in Figures 9e–9g. The RSL changes at Ocean Sites B4–B7, the maximum height region of the peripheral bulge at $t = 0$ kyr (Figure 9d), show a transgression followed by an RSL drop, which is mainly due to the
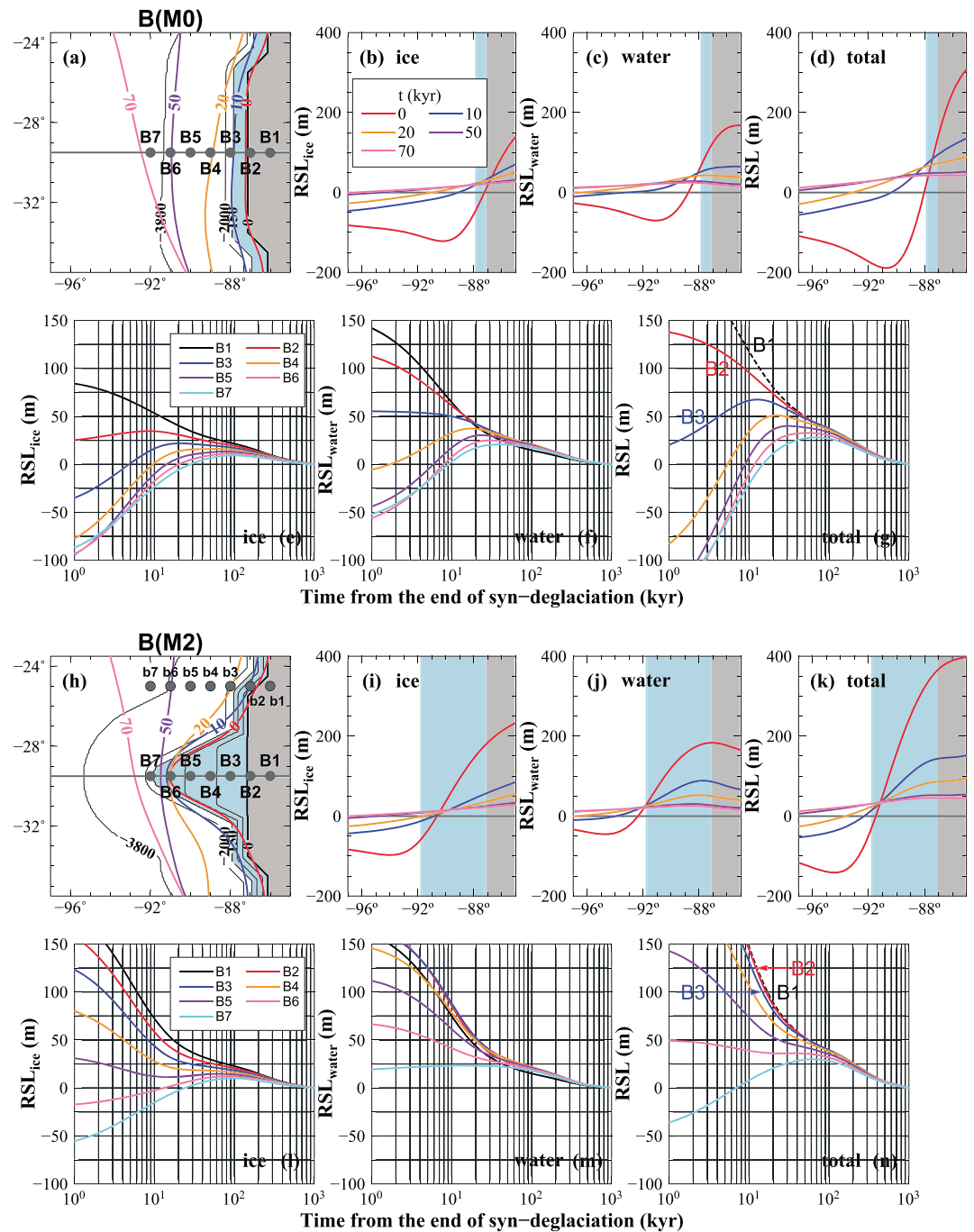
Figure 9. (a) Hinge lines at $t = 0$, 10, 20, 50, and 70 kyr for Region B (see Figure 5a). The predictions are based on the model with $T_d = 2$ kyr, $H = 65$ km, $\eta_{um} = 4 \times 10^{20}$ Pa s, $\eta_{lm} = 5 \times 10^{22}$ Pa s and Coastline Geometry Model M0. The shaded blue region represents the continental shelf for the initial topography, and the gray region represents land area. The contour line for the initial topography is shown by the black line. (b–d) RSL_{ice} and RSL_{water} terms and RSL changes at $t = 0$, 10, 20, 50, and 70 kyr for the transect (dark gray line) shown in panel (a). (e–g) RSL_{ice} and RSL_{water} terms and RSL changes at Sites B1–B7 shown in panel (a). In panel (g), the RSL change predicted at ocean site for the paleotopography is shown by the solid line, and that at land site is shown by the dotted line. The predictions in panels (e) and (f) are shown by solid lines. (h–n) As in panels (a)–(g) except for the Coastline Geometry Model M2.

RSL_{ice} term (e.g., Cathles, 1975). The prediction at Coastline Site B2 for the initial topography shows a continuous RSL fall in "ocean areas," which is largely due to the RSL_{water} term. The RSL change at Site B3 is equally contributed by RSL_{ice} and RSL_{water} terms. These spatial variations are attributed to the

outward migration of hinge line associated with the collapse of the peripheral bulge, resulting in a typical RSL pattern along lines that cross the coastline (Creveling & Mitrovica, 2014).

Paleogeographic reconstructions following Marinoan snowball Earth in Namibia (C in Figure 4a) suggest that the lateral distance of the cap dolostone deposition may have extended longer than 100 km over shallow platforms (Hoffman, 2011). We therefore examine the postdeglacial RSL change for the Coastline Geometry Model M2 with a peninsula described by width and length of (4°, 4°; Figure 9h). The RSL changes are affected by local crustal uplift (RSL fall) associated with ice load melting in the peninsula area and crustal movement due to the hinge-line motions (Figure 9h). Those at Sites b1–b7 are almost the same as those at Sites B1–B7 for M0, respectively, as inferred from the hinge-line movement. The migration rate of the hinge line exhibits significant spatial variability for $t \leq 20$ kyr and the hinge line at the tip of peninsula is nearly stationary until ~20 kyr. However, the migration rate after ~20 kyr is spatially uniform. Also, RSL changes at Sites B1–B7 after $t \sim 20$ kyr are nearly identical to those for M0 (Figures 9g and 9n). These spatial variations in RSL change are explained by considering the interaction between the collapse of the peripheral bulge and local crustal uplift within the peninsula area. We examine these variations by considering the effects of RSL_{ice} and RSL_{water} terms on RSL change.

The maximum height of the peripheral bulge at $t = 0$ kyr moves westward (Figure 9k) locally as inferred from the hinge-line movement at Sites b1–b7 in Figure 9h, and consequently, the peninsula region locally uplifts $t < 20$ kyr. However, the RSL_{ice} and RSL_{water} terms for $t > 20$ kyr at Sites B1–B7 are insensitive to the coastline geometry model (see Figures 9e and 9f, and 9l and 9m), and therefore, the RSL changes after $t \sim 20$ kyr for M2 are nearly identical to those for M0 (Figures 9g and 9n). Figure 9l shows that the RSL_{ice} term for $t < 20$ kyr is significantly affected by the melting in the peninsula and the RSL_{ice} terms at Sites B1–B4 monotonically fall for $t > 0$ kyr (see also Figure 9e). Also, the RSL_{water} term for M2 at Sites B1–B6 shows a fall in the postdeglacial phase (Figure 9m) as is predicted at Sites B1–B3 for M0 (Figure 9f). These effects for $t < 20$ kyr due to the RSL_{ice} and RSL_{water} terms are limited to the peninsula region, and consequently, the RSL changes at Continental Shelf Sites B2–B6 show a gradual RSL fall in ocean area (Figure 9n). That is, the RSL changes at Sites B1–B7 for $t \leq 20$ kyr reflect mainly the local crustal uplift and those for $t > 20$ kyr reflect the behavior of the peripheral bulge for $t > 20$ kyr almost identical to that for M0.

We next examine the RSL change for Region C based on the Coastline Geometry Model M0 (Figures 10a–10g). The difference between Regions C and B (Figure 4a) is due to the spatial scale of the adjacent ocean. Region C faces a relatively small ocean surrounded by continents (ocean "X"). The hinge line shows an inward migration for $t \geq 0$ kyr and the RSL changes bear similar RSL patterns as shown in Figure 6b. The maximum height of the peripheral bulge at $t = 0$ kyr inferred from the RSL change is ~450 m around $-6°$E (Figure 10d) and significantly higher than ~200 m in Region B for M0 (Figure 9d). Particularly, the height for RSL_{water} term (Figure 10c) is ~250 m (~200 m for RSL_{ice} term) and significantly higher than ~70 m in Region B for M0 (Figure 9c). This probably depends on the magnitude of the peripheral bulge at the maximum glaciation and the collapse of the peripheral bulge in the synglacial and postglacial phases. The peripheral bulge at the maximum glaciation is related to the Earth response to the ice loading and seawater unloading, and the collapse of the peripheral bulge in the syndeglacial and postglacial phases is caused by the ice sheet unloading and meltwater loading. That is, the significant contribution of the RSL_{water} term is probably attributed to the GIA response due to the seawater unloading and meltwater loading with a spatial scale of ocean "X" (Figure 5c). This would be a main cause of the inward migration of the hinge line for Region C responsible for the difference between the RSL changes for Regions B and C.

We next examine the RSL change at each site shown in Figures 10e and 10f. The RSL change at inland Site C4 shows a monotonic RSL fall, which is largely contributed by the RSL_{ice} component. Those at Ocean Sites C7–C11 show a transgression followed by an RSL drop, which is equally contributed by the RSL_{ice} and RSL_{water} terms. The RSL changes at Ocean Sites B4–B7 are, however, mainly due to the RSL_{ice} term (Figures 9b and 9c, and 9e and 9f). The prediction at Coastline Site C7 shows a gradual transgression until ~100 kyr (on "land area" for $t < 30$ kyr), which is significantly different from that at Coastline Site B2 (see also RSL changes at Sites B3 and C8). Also, the RSL change at Site C6 shows a nonmonotonic RSL behavior characterized by an RSL drop for $t < 20$ kyr and a transgression for $t > 20$ kyr on "land area," which is mainly contributed by RSL_{water} component (Figure 10f). These differences between the RSL changes for
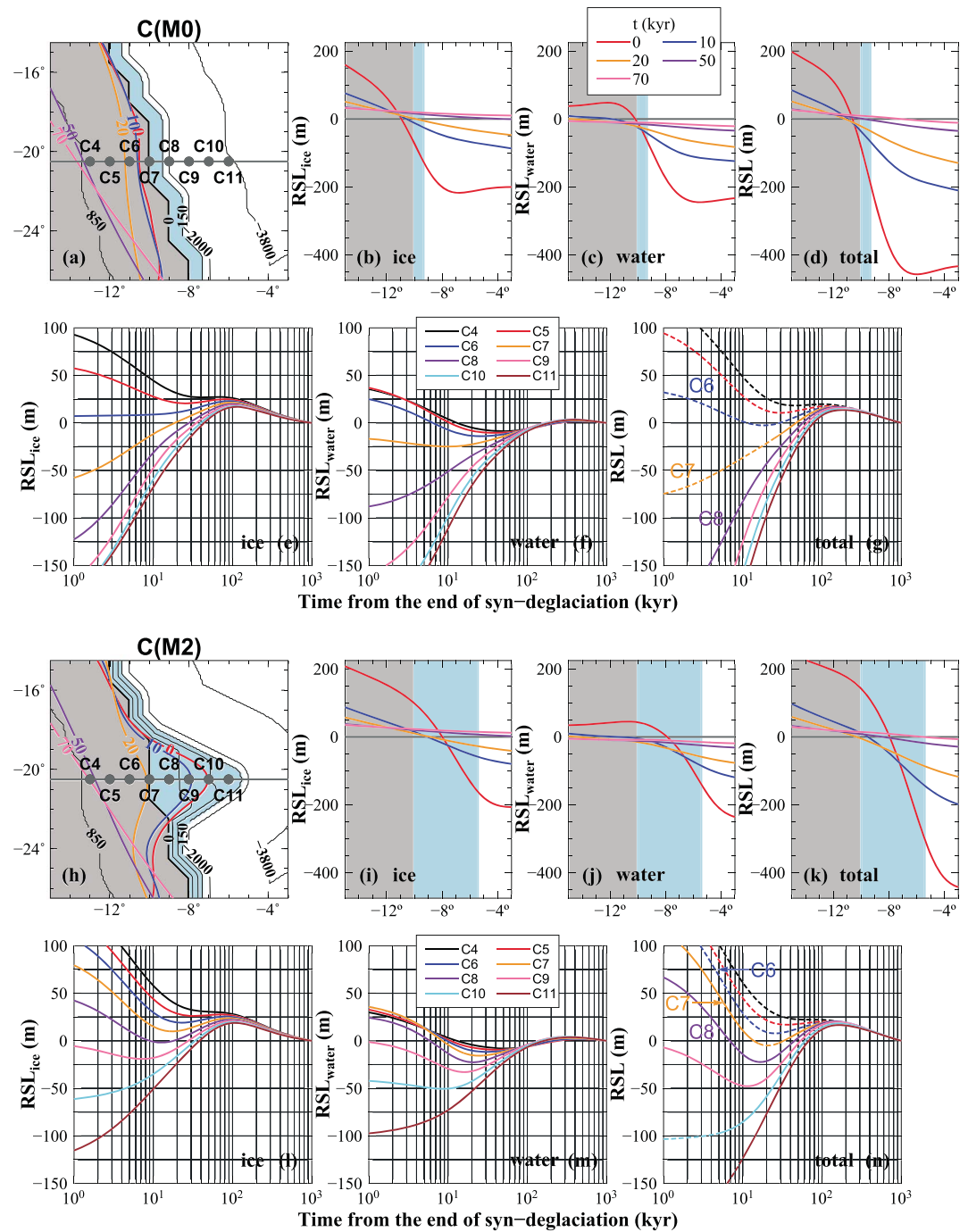
Figure 10. As in Figure 9 except for Region C (see Figure 5a).

Regions B and C are related to the crustal movements around their coastline areas that reflect different hinge-line behaviors (Figures 9a, 10a, and 5c). Also, we point out that Region B, a coastal area in the case of the geometry M0, may be a more suitable depositional place for cap dolostones than that for Region C (see RSL changes at Sites B2 and C7).

We next consider the RSL changes for Region C based on the Coastline Geometry Model M2 (Figures 10h–10n). The RSL changes for $t > 20$ kyr at all Region C sites are nearly identical to those for M0 (Figure 10g) as inferred from the hinge-line movements after $t \sim 20$ kyr for both geometry models (Figures 10a and 10h). Of course, the RSL_{ice} and RSL_{water} contributions for M2 are nearly the same as

those for M0 (Figures 10e and 10f, and 10l and 10m). However, the RSL changes at Sites C7–C9 located on the continental shelf show a nonmonotonic RSL behavior characterized by a significant RSL drop for $t < 20$ kyr followed by a transgression (Figure 10n), which reflects the local hinge-line movement in the peninsula region. The RSL_{ice} term for $t < 20$ kyr is significantly affected by the local uplift associated with ice load melting in the peninsula, which contributes to an RSL drop followed by transgression at Sites C6–C9 (Figures 10l and 10n). The RSL_{water} terms at Sites C4–C6 (continent sites for the initial topography) are nearly the same as those for M0. However, those at Sites C7–C11 for $t < 20$ kyr are significantly larger than those for M0 (Figures 10f and 10m), which also contributes to an RSL drop followed by transgression at Sites C7–C9. Consequently, the RSL changes at Sites C7–C9 show an RSL drop followed by transgression for the continental shelf (Figure 10n). That is, relaxation processes for $t < 20$ kyr are controlled primarily by ice load melting with a spatial scale of the peninsula for M2 (Figures 10l and 10m) and subsequently by the ice sheet unloading and meltwater loading with a spatial scale of the ocean "X." The RSL drops occur within ocean area (denoted by the solid line), and Site C7 lies above sea level from 20 to 30 kyr (denoted by the dotted line). We also point out that such nonmonotonic postdeglacial RSL behavior would not be expected if we evaluate the RSL change relative to a reference time ~10 kyr after the complete melt, corresponding to the postdeglacial RSL change in the case of the post-LGM deglaciation.

We have also examined the predicted postdeglacial RSL changes for other viscosity models in terms of the monotonic and nonmonotonic RSL behaviors described above. The RSL behaviors for M0 and in Region B sites for M2 do not change when other viscosity models are considered, although we do not show the results. In Region C sites for M2, however, nonmonotonic RSL behavior is predicted by several viscosity models. We therefore briefly discuss the postdeglacial RSL changes at Region C sites for M2. Figures 11b–11d show RSL changes at Sites C7–C11 for three lower mantle viscosity models. The general feature of the RSL change for $\eta_{lm} = 5 \times 10^{21}$ Pa s (Figure 11b) is similar to that for $\eta_{lm} = 10^{22}$ Pa s (Figure 11c) and an RSL drop followed by transgression is not evident for these models. Figure 11d shows the RSL changes for a two-layer lower mantle viscosity model with $\eta_{670,1191} = 5 \times 10^{21}$ and $\eta_{1191,2891} = 5 \times 10^{22}$ Pa s. This two-layer model predicts an RSL drop followed by transgression at Sites C7–C9, a trend that is also predicted for the model with $\eta_{lm} = 5 \times 10^{22}$ (Figure 10n). That is, the sea level peak at ~100 kyr predicted for these two viscosity models, which is largely driven by the ice sheet unloading and meltwater loading with a spatial scale of the ocean "X," can be attributed mainly to the viscosity in the deep mantle, that is, the viscosity below 1,191-km depth assumed in this study. Although we only show the results for $T_d = 2$ kyr, the sensitivity of the postdeglacial RSL change to the lower mantle viscosity is also evident for the cases of $T_d > 2$ kyr.

Figures 11e–11h explore the sensitivities of predicted RSL changes to the lithospheric thickness (H), upper mantle viscosity (η_{um}), and syndeglacial duration (T_d) in the case of the two-layer lower mantle viscosity model. For the models with $T_d = 2$ and 5 kyr, a postdeglacial RSL drop followed by transgression is predicted for all upper mantle viscosity models. For the models with $T_d = 7.5$ and 10 kyr, however, a nonmonotonic RSL behavior is predicted for $4 \times 10^{20} < \eta_{um} \leq 7 \times 10^{20}$ Pa s (Figures 11e–11g). These results are related to the trade-off between T_d and η_{um} values. In the case of the model with $T_d = 10$ kyr and $\eta_{um} = 2 \times 10^{20}$ Pa s, for example, the peninsula-scale viscous relaxation occurs largely in the syndeglacial phase and its related crustal uplift has a negligible impact on the postdeglacial RSL change. Figure 11h shows the sensitivity to the lithospheric thickness. The general feature of the RSL change for $H = 100$ km is similar to that evident for $H = 65$ km. However, an RSL drop is not predicted for $H = 200$ km because the crustal deformation with a spatial scale of peninsula for M2 is elastically supported by the thick lithosphere.

4. Discussion

4.1. Comparison Between Sedimentary-Inferred and Predicted RSL Changes

Marinoan cap dolostones are generally accepted to have been deposited during the marine transgression resulting from snowball meltdown (Hoffman & Schrag, 2002). The transgression is mainly caused by an ESL rise in the syndeglacial phase (e.g., RSL change at Site C3 in Figure 3b) and by collapse of peripheral bulge in the postdeglacial phase (e.g., RSL change at Site B3 in Figure 9g), as demonstrated by Creveling and Mitrovica (2014). Indeed, postmeltdown sedimentary records such as cap dolostones appear to reflect transgression alone in, for example, southern Amazon (Nogueira et al., 2007), Zavkhan Terrane of
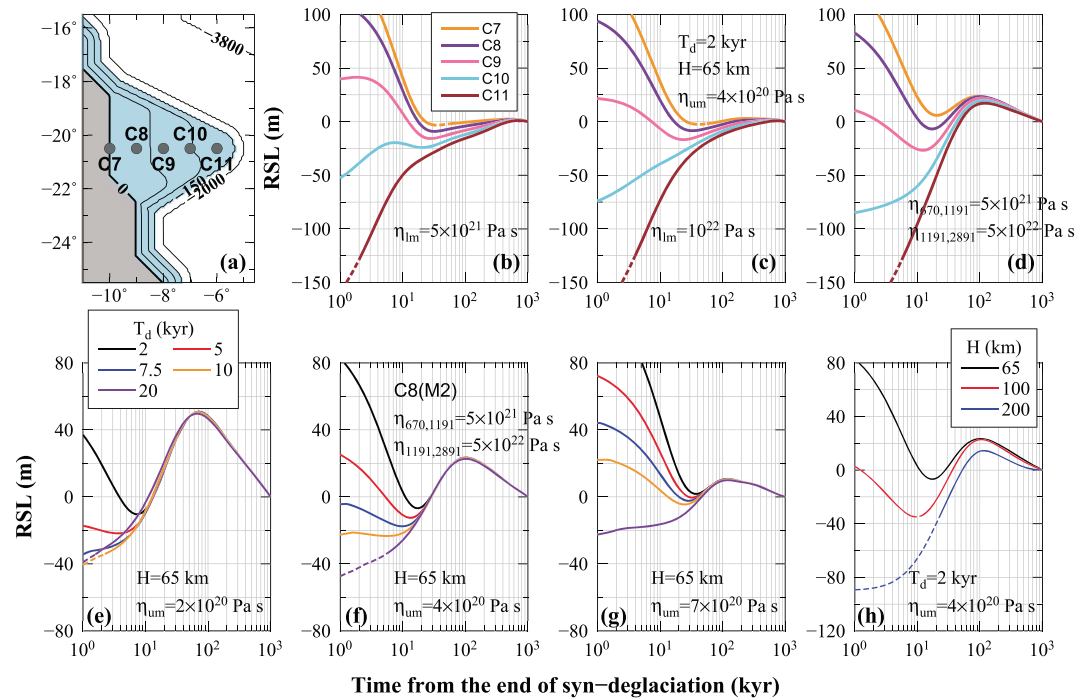
Figure 11. (a) An enlarged map for Region C with the Coastline Geometry Model M2. The shaded blue region represents the continental shelf for the initial topography and the gray regions represent land areas. The contour line for the initial topography is shown by the black line. (b–d) Relative sea level (RSL) changes at Sites C7–C11 in panel (a) for $T_d = 2$ kyr, $H = 65$ km, and $\eta_{um} = 4 \times 10^{20}$ Pa s (thick line). (b and c) RSL changes for simple three-layer viscosity models with $\eta_{lm} = (5, 10) \times 10^{21}$ Pa s and (d) RSL changes for a two-layer lower mantle viscosity model with $\eta_{670,1191} = 5 \times 10^{21}$ and $\eta_{1191,2891} = 5 \times 10^{22}$ Pa s. (e–h) RSL changes at Site C8 in panel (a) for the two-layer lower mantle viscosity model. (e–g) RSL changes for $T_d = (2, 5, 7.5, 10, 20)$ kyr, $H = 65$ km, and $\eta_{um} = (2, 4, 7) \times 10^{20}$ Pa s and (h) RSL changes for $T_d = 2$ kyr, $H = (65, 100, 200)$ km, and $\eta_{um} = 4 \times 10^{20}$ Pa s. The RSL change predicted at ocean site for the paleotopography is shown by the solid line, and that at land site is shown by the dotted line.

southwestern Mongolia (Bold et al., 2016), Svalbard (Halverson et al., 2004) and East Finnmark of Norway (Rice et al., 2011; AM, MO, SV, and NO in Figure 5a, respectively). However, an RSL drop interrupting transgression has been identified in some regions. Stratigraphic records show a syndeglacial RSL drop in Namibia (Hoffman & Macdonald, 2010) and South Australia (Rose et al., 2013; NA and SA in Figure 5a, respectively). Creveling and Mitrovica (2014) indicated that such a syndeglacial RSL drop may be attributed to one of the three processes (or their combination) of rapid localized (asynchronous) melting during a global stasis in melting, crustal uplift in regions previously under significant ice cover, and an extended syndeglacial phase of duration ~50 kyr or greater. In this study, syndeglacial RSL drop is predicted at the continental slope site for the coastline geometry models M1 and M2 (Figure 3). This is related to the second process discussed by Creveling and Mitrovica (2014).

On the other hand, nonmonotonic RSL behavior in the postdeglacial phase characterized by an RSL drop and a resumed transgression has been inferred from cap dolostones on the continental shelf of locations such as the south China. Our numerical experiments indicate that the nonmonotonic postdeglacial RSL behavior is sensitive to the syndeglacial duration, mantle viscosity structure, and paleogeography. That is, it may be possible to put some constraints on these model parameters by comparing sedimentary-inferred and predicted RSL changes at different sites. Any such inferences are bound to be preliminary given the sparsity of observationally inferred RSL changes and uncertainties in GIA modeling parameters associated with melting histories and paleogeography. However, the following discussion is valid even if we adopt a rapid localized melting event. That is, a rapid localized melting event has a minor impact on the postdeglacial RSL change because this change is mainly driven by the relaxation process due to the continent-scale deglaciation rather than by the localized melting. It is also noted that the postdeglacial RSL change in south

China, which is significantly affected by Earth's rotational response to Marinoan snowball meltdown, is thus mainly sensitive to gross melting history.

Zhou et al. (2010) inferred an RSL change with a syndeglacial transgression followed by an RSL drop and a transgression in the postdeglacial phase based on the stratigraphic studies of cap dolostones in south China (SC in Figure 5a). They interpreted the karst-like dissolution features at the top of the cap dolostones as a brief interval of RSL drop, which are common throughout most of the platform, shelf, and even shallow basinal facies in south China. Over the continental shelf area between Sites A1 and A2 (Figure 7a), syndeglacial transgression followed by an RSL drop and transgression in the postdeglacial phase is predicted for models with a viscosity of 5×10^{22} Pa s in the deep mantle and $T_d \leq 20$ kyr regardless of the adopted upper mantle viscosity and lithospheric thickness (Figure 7). The predicted RSL change is consistent with the inferred RSL change in south China although only the coastal region between Sites A1 and A4 (Figure 7a) undergoes subaerial exposure.

The cap dolostones on shelf sections in Mackenzie Mountains, northwestern Canada (James et al., 2001; MM in Figure 5a) and on the topographic highs in West Africa (Bertrand-Sarfati et al., 1997; Shields et al., 2007; WA in Figure 5a) suggest similar sedimentary features as those of the cap carbonate sequences in south China. Also, the cap carbonate platform in California (CA in Figure 5a) records karstic features (Creveling et al., 2016). The karst features at these sites have been interpreted as an RSL drop in the syndeglacial phase due to glacial rebound. However, our numerical experiments do not predict the syndeglacial RSL drop for ocean sites of the continental shelf because the continental shelf lies above sea level until the late stage of the syndeglacial phase. However, our model suggests that the inferred RSL drop may have occurred during the postdeglacial phase, which is consistent with the cap dolostones at these sites bearing no ice-rafted debris. Differing from south China, the RSL changes of Canada and California sites had a negligible signal from Earth's rotation because they were at equatorial regions. The same may be true for the West Africa site (see Figure 4d).

Our numerical experiments indicate that nonmonotonic postdeglacial RSL behavior requires the following two paleogeographic conditions: (i) an adjacent ocean such as the ocean "X" or oceans (gulfs) indicated by arrows in Figure 5c and (ii) a wide continental shelf such as M2 (Figure 10h). We therefore discuss the RSL drop at these sites based on the postdeglacial RSL changes at Continental Shelf Site C8 for the geometry model M2 (Figure 10h). We found that an RSL drop followed by transgression in the postdeglacial phase is evident for models with a viscosity of 5×10^{22} Pa s in the deep mantle and $T_d < 20$ kyr and also depends on the upper mantle viscosity (Figure 11). It should be noted that the predicted RSL change in Region C is significantly affected by the subsidence of the ocean "X" due to the ice sheet unloading and meltwater loading. The northwestern Canada (MM) and West Africa (WA) sites (Figure 5a), which face an ocean (gulf) indicated by arrows in Figure 5c, show nonmonotonic RSL behaviors for the Coastline Geometry Model M2 as inferred from the RSL changes for Region C (Figures 5, 10, and 11). Also, it may be possible to assume that the paleogeography around the California (CA) site (Figure 5a) had a comparable geometry to that for Region C if we consider uncertainties of the paleogeography (see paleogeography around California site).

The nonmonotonic postdeglacial RSL behavior inferred from the sedimentary records worldwide may be explained by a synchronous melting model with $T_d < 20$ kyr and a deep mantle viscosity of $\sim 5 \times 10^{22}$ Pa s. A discussion of Neoproterozoic mantle viscosity is challenging if we consider the thermal history of the Earth (e.g., Ganne & Feng, 2017) and its impact on the mantle viscosity (Karato, 2008). Nevertheless, a deep mantle viscosity of $\sim 5 \times 10^{22}$ Pa s may be consistent with an estimate of $\sim 10^{23}$ Pa s inferred from the recent analyses using GIA data sets pertinent to the last deglaciation (Lau et al., 2016; Nakada et al., 2018; Nakada & Okuno, 2016). According to the results of Ganne and Feng (2017), for example, the average temperature of the mantle at 0.6–0.7 Gyr was ~50 K higher than at present. This may suggest that the Neoproterozoic mantle viscosity is approximately half of the present one for an assumed temperature distribution by Nakada et al. (2018). Nakada et al. (2018) examined the GIA-related observations such as RSL changes and secular rate of change of the degree-two zonal harmonic of the geopotential, $\dot{J}_2$, based on the temperature-dependent viscosity model. Although the results are not shown here, the nonmonotonic postdeglacial RSL behavior inferred from the sedimentary records worldwide can be explained based on the viscosity model with temperature distribution ~50 K higher than the deep mantle viscosity of 10^{23} Pa s and average upper mantle
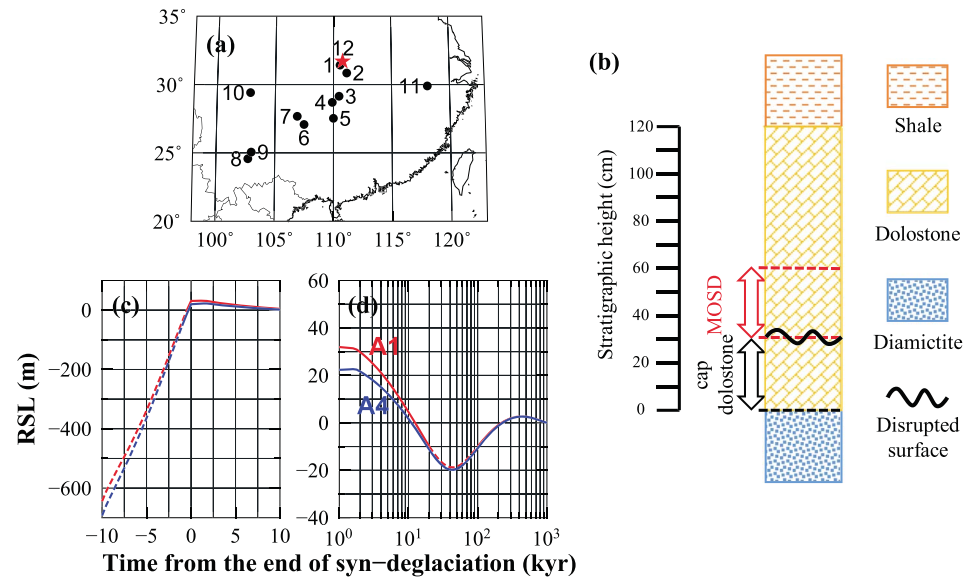
Figure 12. (a) Marinoan cap dolostone sections on south China (or Yangtze) craton: Sections 1–11 investigated by Zhou et al. (2010) and Section 12 investigated by Killingsworth et al. (2013). (b) The post-Marinoan or basal Ediacaran stratigraphic sequence at Wushanhu (Section 12), Hubei Province, China (modified from Killingsworth et al., 2013). (c and d) Syndeglacial and postdeglacial RSL changes at Sites A1 and A4 (Figure 7a) for the model with $T_d = 10$ kyr, $H = 65$ km, $\eta_{um} = 4 \times 10^{20}$, $\eta_{670,1191} = 5 \times 10^{21}$, and $\eta_{1191,2891} = 5 \times 10^{22}$ Pa s. The RSL change predicted at ocean site for the paleotopography is shown by the solid line, and that at land site is shown by the dotted line. MOSD = Marinoan ^{17}O depletion; RSL = relative sea level.

viscosity of 4×10^{20} Pa s preferred by Nakada et al. (2018). A postdeglacial RSL drop followed by transgression is also predicted for the viscosity model with an upper mantle viscosity of 10^{20} Pa s and lithospheric thickness of 50 km as inferred from the results shown in Figures 7e–7h and 11e–11h.

Finally, we discuss the syndeglacial duration. The numerous positive feedbacks in the climate system suggest that once deglaciation begins, it proceeds rapidly to a globally ice-free state (Hoffman et al., 2017; Pierrehumbert et al., 2011). The duration of ~2 kyr has been inferred from ice sheet dynamics (Hyde et al., 2000). For a melting model with $T_d \sim 2$ kyr, syndeglacial RSL drop would be predicted in the case of a melting model with a rapid localized melting event (Creveling & Mitrovica, 2014). More recently, Myrow et al. (2018) examined a rate of sea level rise during the deglaciation based on a paleohydraulic analysis of wave ripples and tidal laminae for ~100-year sediment records of the Elatina Formation, South Australia (SA in Figure 2a), and estimated a rate equivalent to a syndeglacial duration of ~6 kyr. Our estimate of $T_d < 20$ kyr inferred from nonmonotonic RSL behavior in the postdeglacial phase is not inconsistent with these estimates, but we cannot put a tight constraint on the syndeglacial duration.

4.2. Inference of MOSD Duration

Our modeling exercise allows us to place some constraints on the duration of the MOSD event, a transient episode of extremely ^{17}O-depleted atmospheric O_2, recorded in the sediments immediate after the onset of the Marinoan meltdown. Figure 12a shows Marinoan cap dolostone sections on south China craton (Jiang et al., 2011; Killingsworth et al., 2013; Zhou et al., 2010), and Figure 12b shows the Nantuo diamictites and a basal Ediacaran stratigraphic sequence at Wushanhu (Section 12 in Figure 12a), Hubei Province, China. Zhou et al. (2010) and Killingsworth et al. (2013) define the cap carbonates as the carbonates overlying the Nantuo diamictite that deposited before the occurrence of a disrupted (dissolution or karst) surface that hosts barite crystal fans. The disrupted features at the top of the cap carbonates are common throughout most of the platform, shelf, and even shallow basinal facies in south China (Zhou et al., 2010; Sections 1–11 in Figure 12a). Therefore, if we can correlate the sedimentologically inferred sea level change to the Wushanhu section where the MOSD has been pinned to the postmeltdown sedimentary sequence (Killingsworth et al., 2013; Section 12 in Figure 12a), we can provide an independent estimate of the

duration of the cap carbonate deposition, the timing of the barite fan deposition, and the duration of the MOSD event, based on our modeled RSL pattern and durations. The MOSD signature is recorded by sulfate deposits such as the unusual barite fans (Bao et al., 2008). Since the MOSD window is not coeval with the time of the highest pCO_2 when the meltdown began but rather a time when the atmospheric O_2 and CO_2 had comparable concentrations (Cao & Bao, 2013), the MOSD duration can provide an important constraint on the rates of pCO_2 drawdown by weathering and pO_2 rise due to biological recovery and organic burial in the aftermath of Marinoan snowball meltdown.

Figures 12c and 12d show the RSL changes at Sites A1 and A4 (Figure 7a) based on the model with $T_d = 10$ kyr (see also Figure 7). The Nantuo diamictites should have been deposited by the end of the syndeglacial transgression. If the predicted postdeglacial RSL drop or regression-transgression transition occurred at the top of the cap carbonates or at the onset of the barite fan deposition, the inferred period for cap carbonate deposition (Figure 12b) would be ~50 kyr (Figure 12d). Also, if we assume that the deposition of the cap carbonates in south China started at the end of syndeglacial phase, the maximum duration of the cap carbonate deposition would also be ~50 kyr. If an equal deposition rate for the cap dolostones and the overlying dolostones, where the MOSD period resides, is assumed, the maximum duration of the MOSD is also estimated to be also ~50 kyr. If we consider Le Hir et al.'s (2008) ocean chemistry constraint that it would take a minimum of 20 kyr to bring the ocean alkalinity to the level of carbonate precipitation via continental weathering, then the corresponding durations of the cap carbonate deposition and the MOSD event will both be 30 kyr. These estimates are consistent with the previous estimate of a <1 Myr duration for the MOSD event, as inferred independently from two radiometric dates for nearby sections correlated to the Wushanhu section (Killingsworth et al., 2013), and also from a coupled, four-box, and quick-response biosphere-atmosphere model (Cao & Bao, 2013). Added the <20-kyr syndeglacial duration, the total duration starting from the onset of deglaciation to the end of the MOSD episode is within 100 kyr. The 100 kyr is therefore the total time the post-Marinoan Earth took to draw a pCO_2 at >100 present atmospheric level down to a level within 1–2 magnitudes of present atmospheric level.

5. Conclusions

Marinoan snowball Earth offers us a set of sedimentary and geochemical records for exploring GIA associated with one of the most severe glaciations in Earth history. Moreover, an accurate prediction of GIA-based RSL change associated with a snowball Earth will help to interrogate sedimentary records to place constraints on mantle viscosity structure, the paleogeographic details associated with cap carbonate deposition, and the durations of syndeglaciation and cap carbonate deposition. We have assumed a globally synchronous melting for all ice sheets and have evaluated GIA-based RSL changes by considering the impacts of paleotopography and coastline geometry on inferred GIA model parameters. The main purpose of this study is to discuss the postdeglacial RSL change characterized by an RSL drop followed by a transgression inferred from sedimentary records such as those in south China (Zhou et al., 2010). This is because such a nonmonotonic RSL behavior may be a diagnostic suggesting that the Marinoan deglaciation was characterized by a significantly longer postdeglacial GIA response than the last deglaciation. A postdeglacial RSL drop followed by transgression in south China, which is significantly impacted by changes in Earth's rotation, is predicted over the continental shelf area for models with $T_d \leq 20$ kyr and a deep mantle viscosity of ~5×10^{22} Pa s regardless of the adopted upper mantle viscosity and lithospheric thickness (Figure 7). On the other hand, postdeglacial RSL changes at low-latitude regions (e.g., NA, MM, and CA sites in Figure 5a), having a negligible RSL contribution from Earth rotation, are driven largely by the collapse of the peripheral bulge and also by paleogeographic considerations, such as the scale of adjacent ocean and size of the continental shelf. Our GIA modeling of the RSL change in south China also explains the sedimentary-inferred RSL drops on the continental shelf in northwestern Canada (James et al., 2001) and California (Creveling et al., 2016) if these sites were adjacent to an ocean such as the ocean "X" (oceans in Figure 5c indicated by arrows) and located on a wide continental shelf such as in the geometry model M2 (Figures 10 and 11). Furthermore, the good match between the predicted and the observed RSL change in south China suggests an approximate duration of ~50 kyr for the MOSD event, an atmospheric event linked to the post-Marinoan drawdown of CO_2 and the concurrent rise of O_2 (Figure 12).

References

Bao, H., Lyons, J. R., & Zhou, C. (2008). Triple oxygen isotope evidence for elevated CO_2 levels after a Neoproterozoic glaciation. *Nature*, *453*(7194), 504–506. https://doi.org/10.1038/nature06959

Bertrand-Sarfati, J., Flicoteaux, R., Moussine-Pouchkine, A., & Ait Kaci Ahmed, A. (1997). Lower Cambrian apatitic stromatolites and phospharenites related to the glacio-eustatic cratonic rebound (Sahara, Algeria). *Journal of Sedimentary Research*, *67*(5), 957–974. https://doi.org/10.1306/D426868A-2B26-11D7-8648000102C1865D

Bold, U., Smith, E. F., Rooney, A. D., Bowring, S. A., Buchwaldt, R., Dudas, F., et al. (2016). Neoproterozoic stratigraphy of the Zavkhan terrane of Mongolia: The backbone for Cryogenian and early Ediacaran chemostratigraphic records. *American Journal of Science*, *316*(1), 1–63. https://doi.org/10.2475/01.2016.01

Cao, X., & Bao, H. (2013). Dynamic model constraints on oxygen-17 depletion in atmospheric O_2 after a snowball Earth. *Proceedings of the National Academy of Sciences*, *110*(36), 14,546–14,550. https://doi.org/10.1073/pnas.1302972110

Cathles, L. M. (1975). *The viscosity of the Earth's mantle*. Princeton, NJ: Princeton University Press.

Clark, J. A. (1976). Greenland's rapid postglacial emergence: A result of ice-water gravitational attraction. *Geology*, *4*(5), 310–312. https://doi.org/10.1130/0091-7613(1976)4<310:GRPEAR>2.0.CO;2

Creveling, J. R., Bergmann, K. D., & Grotzinger, J. P. (2016). Cap carbonate platform facies model, Noonday Formation, SE California. *Bulletin of the Geological Society of America*, *128*(7-8), 1249–1269. https://doi.org/10.1130/B31442.1

Creveling, J. R., & Mitrovica, J. X. (2014). The sea-level fingerprint of a Snowball Earth deglaciation. *Earth and Planetary Science Letters*, *399*, 74–85. https://doi.org/10.1016/j.epsl.2014.04.029

Dziewonski, A. M., & Anderson, D. L. (1981). Preliminary reference Earth model. *Physics of the Earth and Planetary Interiors*, *25*(4), 297–356. https://doi.org/10.1016/0031-9201(81)90046-7

Farrell, W. E., & Clark, J. A. (1976). On postglacial sea level. *Geophysical Journal of the Royal Astronomical Society*, *46*(3), 647–667. https://doi.org/10.1111/j.1365-246X.1976.tb01252.x

Ganne, J., & Feng, X. (2017). Primary magmas and mantle temperatures through time. *Geochemistry, Geophysics, Geosystems*, *18*, 872–888. https://doi.org/10.1002/2016GC006787

Halverson, G. P., Maloof, A. C., & Hoffman, P. F. (2004). The Marinoan glaciation (Neoproterozoic) in northeast Svalbard. *Basin Research*, *16*(3), 297–324. https://doi.org/10.1111/j.1365-2117.2004.00234.x

Hoffman, P. F. (2011). Strange bedfellows: Glacial diamictite and cap carbonate from the Marinoan (635 Ma) glaciation in Namibia. *Sedimentology*, *58*(1), 57–119. https://doi.org/10.1111/j.1365-3091.2010.01206.x

Hoffman, P. F., Abbot, D. S., Ashkenazy, Y., Benn, D. I., Brocks, J. J., Cohen, P. A., et al. (2017). Snowball Earth climate dynamics and Cryogenian geology-geobiology. *Science Advances*, *3*(11), e1600983. https://doi.org/10.1126/sciadv.1600983

Hoffman, P. F., Halverson, G. P., Domack, E. W., Husson, J. M., Higgins, J. A., & Schrag, D. P. (2007). Are basal Ediacaran (635 Ma) post-glacial "cap dolostones" diachronous? *Earth and Planetary Science Letters*, *258*(1–2), 114–131. https://doi.org/10.1016/j.epsl.2007.03.032

Hoffman, P. F., & Li, Z. X. (2009). A palaeogeographic context for Neoproterozoic glaciation. *Palaeogeography, Palaeoclimatology, Palaeoecology*, *277*(3–4), 158–172. https://doi.org/10.1016/j.palaeo.2009.03.013

Hoffman, P. F., & Macdonald, F. A. (2010). Sheet-crack cements and early regression in Marinoan (635Ma) cap dolostones: Regional benchmarks of vanishing ice-sheets? *Earth and Planetary Science Letters*, *300*(3-4), 374–384. https://doi.org/10.1016/j.epsl.2010.10.027

Hoffman, P. F., & Schrag, D. P. (2002). The snowball Earth hypothesis: testing the limits of global change. *Terra Nova*, *14*(3), 129–155. https://doi.org/10.1046/j.1365-3121.2002.00408.x

Hyde, W. T., Crowley, T. J., Baum, S. K., & Peltier, W. R. (2000). Neoproterozoic "snowball earth" simulations with a coupled climate/ice-sheet model. *Nature*, *405*(6785), 425–429. https://doi.org/10.1038/35013005

James, N. P., Narbonne, G. M., & Kyser, T. K. (2001). Late Neoproterozoic cap carbonates: Mackenzie Mountains, northwestern Canada: Precipitation and global glacial meltdown. *Canadian Journal of Earth Sciences*, *38*(8), 1229–1262. https://doi.org/10.1139/cjes-38-8-1229

Jiang, G., Shi, X., Zhang, S., Wang, Y., & Xiao, S. (2011). Stratigraphy and paleogeography of the Ediacaran Doushantuo Formation (ca. 635–551 Ma) in South China. *Gondwana Research*, *19*(4), 831–849. https://doi.org/10.1016/j.gr.2011.01.006

Karato, S. (2008). *Deformation of earth materials: An introduction to the rheology of solid earth*. Cambridge: Cambridge University Press. https://doi.org/10.1017/CBO9780511804892

Killingsworth, B. A., Hayles, J. A., Zhou, C., & Bao, H. (2013). Sedimentary constraints on the duration of the Marinoan Oxygen-17 Depletion (MOSD) event. *Proceedings of the National Academy of Sciences*, *110*(44), 17,686–17,690. https://doi.org/10.1073/pnas.1213154110

Kilner, B., Mac Niocaill, C., & Brasier, M. (2005). Low-latitude glaciation in the Neoproterozoic of Oman. *Geology*, *33*(5), 413–416. https://doi.org/10.1130/G21227.1

Lambeck, K. (1993). Glacial rebound of the British Isles—I. Preliminary model results. *Geophysical Journal International*, *115*(3), 941–959. https://doi.org/10.1111/j.1365-246X.1993.tb01503.x

Lambeck, K. (1997). Sea-level change along the French Atlantic and Channel coasts since the time of the Last Glacial Maximum. *Palaeogeography, Palaeoclimatology, Palaeoecology*, *129*(1–2), 1–22. https://doi.org/10.1016/S0031-0182(96)00061-2

Lambeck, K., & Johnston, P. (1998). The viscosity of the mantle: evidence from analyses of glacial-rebound phenomena. In I. Jackson (Ed.), *The Earth's mantle: Composition, structure, and evolution* (pp. 461–502). Cambridge: Cambridge University Press.

Lambeck, K., Purcell, A., Johnston, P., Nakada, M., & Yokoyama, Y. (2003). Water-load definition in the glacio-hydro-isostatic sea-level equation. *Quaternary Science Reviews*, *22*(2–4), 309–318. https://doi.org/10.1016/S0277-3791(02)00142-7

Lambeck, K., Purcell, A., & Zhao, S. (2017). The North American Late Wisconsin ice sheet and mantle viscosity from glacial rebound analyses. *Quaternary Science Reviews*, *158*, 172–210. https://doi.org/10.1016/j.quascirev.2016.11.033

Lambeck, K., Rouby, H., Purcell, A., Sun, Y., & Sambridge, M. (2014). Sea level and global ice volumes from the Last Glacial Maximum to the Holocene. *Proceedings of the National Academy of Sciences*, *111*(43), 15,296–15,303. https://doi.org/10.1073/pnas.1411762111

Lau, H. C. P., Mitrovica, J. X., Austermann, J., Crawford, O., Al-Attar, D., & Latychev, K. (2016). Inferences of mantle viscosity based on ice age data sets: Radial structure. *Journal of Geophysical Research: Solid Earth*, *121*, 6991–7012. https://doi.org/10.1002/2016JB013043

Le Hir, G., Goddéris, Y., Donnadieu, Y., & Ramstein, G. (2008). A geochemical modelling study of the evolution of the chemical composition of seawater linked to a "'snowball'" glaciation. *Biogeosciences*, *5*(1), 253–267. https://doi.org/10.5194/bg-5-253-2008

Li, Z. X., Evans, D. A. D., & Halverson, G. P. (2013). Neoproterozoic glaciations in a revised global palaeogeography from the breakup of Rodinia to the assembly of Gondwanaland. *Sedimentary Geology*, *294*, 219–232. https://doi.org/10.1016/j.sedgeo.2013.05.016

Liu, Y., & Peltier, W. R. (2013). Sea level variations during snowball Earth formation: 1. A preliminary analysis. *Journal of Geophysical Research: Solid Earth*, *118*, 4410–4424. https://doi.org/10.1002/jgrb.50293

Milne, G. A., & Mitrovica, J. X. (1996). Postglacial sea-level change on a rotating Earth: first results from a gravitationally self-consistent sea-level equation. *Geophysical Journal International*, *126*(3), F13–F20. https://doi.org/10.1111/j.1365-246X.1996.tb04691.x

Milne, G. A., Mitrovica, J. X., & Davis, J. L. (1999). Near-field hydro-isostasy: The implementation of a revised sea-level equation. *Geophysical Journal International*, *139*(2), 464–482. https://doi.org/10.1046/j.1365-246X.1999.00971.x

Mitrovica, J. X., & Forte, A. M. (2004). A new inference of mantle viscosity based upon joint inversion of convection and glacial isostatic adjustment data. *Earth and Planetary Science Letters*, *225*(1–2), 177–189. https://doi.org/10.1016/j.epsl.2004.06.005

Mitrovica, J. X., Wahr, J., Matsuyama, I., & Paulson, A. (2005). The rotational stability of an ice-age earth. *Geophysical Journal International*, *161*(2), 491–506. https://doi.org/10.1111/j.1365-246X.2005.02609.x

Myrow, P. M., Lamb, M. P., & Ewing, R. C. (2018). Rapid sea level rise in the aftermath of a Neoproterozoic snowball Earth. *Science*, *360*(6389), 649–651. https://doi.org/10.1126/science.aap8612

Nakada, M., & Lambeck, K. (1987). Glacial rebound and relative sea-level variations: a new appraisal. *Geophysical Journal of the Royal Astronomical Society*, *90*(1), 171–224. https://doi.org/10.1111/j.1365-246X.1987.tb00680.x

Nakada, M., & Lambeck, K. (1989). Late Pleistocene and Holocene sea-level change in the Australian region and mantle rheology. *Geophysical Journal*, *96*(3), 497–517. https://doi.org/10.1111/j.1365-246X.1989.tb06010.x

Nakada, M., & Lambeck, K. (1991). Late Pleistocene and Holocene sea-level change: evidence for lateral mantle viscosity structure? In R. Sabadini, K. Lambeck, & E. Boschi (Eds.), *Glacial isostasy, sea level and mantle rheology* (pp. 79–94). Dordrecht: Kluwer Academic. https://doi.org/10.1007/978-94-011-3374-6_5

Nakada, M., & Okuno, J. (2016). Inference of mantle viscosity for depth resolutions of GIA observations. *Geophysical Journal International*, *207*(2), 719–740. https://doi.org/10.1093/gji/ggw301

Nakada, M., Okuno, J., & Irie, Y. (2018). Inference of viscosity jump at 670 km depth and lower mantle viscosity structure from GIA observations. *Geophysical Journal International*, *212*(3), 2206–2225. https://doi.org/10.1093/gji/ggx519

Nakada, M., Okuno, J., & Yokoyama, Y. (2016). Total meltwater volume since the Last Glacial Maximum and viscosity structure of Earth's mantle inferred from relative sea level changes at Barbados and Bonaparte Gulf and GIA-induced J_2. *Geophysical Journal International*, *204*(2), 1237–1253. https://doi.org/10.1093/gji/ggv520

Nogueira, A. C. R., Riccomini, C., Sial, A. N., Moura, C. A. V., Trindade, R. I. F., & Fairchild, T. R. (2007). Carbon and strontium isotope fluctuations and paleoceanographic changes in the late Neoproterozoic Araras carbonate platform, southern Amazon craton, Brazil. *Chemical Geology*, *237*(1–2), 168–190. https://doi.org/10.1016/j.chemgeo.2006.06.016

Paterson, W. S. B. (1969). *The physics of glaciers*. Oxford: Pergamon Press.

Pierrehumbert, R. T., Abbot, D. S., Voigt, A., & Koll, D. (2011). Climate of the Neoproterozoic. *Annual Review of Earth and Planetary Sciences*, *39*(1), 417–460. https://doi.org/10.1146/annurev-earth-040809-152447

Rice, A. H. N., Edwards, M. B., Hansen, T. A., Arnaud, E., & Halverson, G. P. (2011). In E. Arnaud, G. P. Halverson, & G. A. Shields-Zhou (Eds.), *Glaciogenic rocks of the Neoproterozoic Smalfjord and Mortensnes formations, Vestertana Group, E. Finnmark, Norway*, *Geological society, London, Memoirs* (Vol. 36, pp. 593–602). London: Geological Society of London. https://doi.org/10.1144/M36.57

Rose, C. V., Maloof, A. C., Schoene, B., Ewing, R. C., Linnemann, U., Hofmann, M., & Cottle, J. M. (2013). The end-Cryogenian glaciation of South Australia. *Geoscience Canada*, *40*(4), 256–293. https://doi.org/10.12789/geocanj.2013.40.019

Shields, G. A., Deynoux, M., Strauss, H., Paquet, H., & Nahon, D. (2007). Barite-bearing cap dolostones of the Taoudéni Basin, northwest Africa: Sedimentary and isotopic evidence for methane seepage after a Neoproterozoic glaciation. *Precambrian Research*, *153*(3–4), 209–235. https://doi.org/10.1016/j.precamres.2006.11.011

Trindade, R. I. F., Font, E., D'Agrella-Filho, M. S., Nogueira, A. C. R., & Riccomini, C. (2003). Low-latitude and multiple geomagnetic reversals in the Neoproterozoic Puga cap carbonate, Amazon craton. *Terra Nova*, *15*(6), 441–446. https://doi.org/10.1046/j.1365-3121.2003.00510.x

Tushingham, A. M., & Peltier, W. R. (1991). Ice-3G: A new global model of Late Pleistocene deglaciation based upon geophysical predictions of post-glacial relative sea level change. *Journal of Geophysical Research*, *96*(B3), 4497–4523. https://doi.org/10.1029/90jb01583

Zhou, C., Bao, H., Peng, Y., & Yuan, X. (2010). Timing the deposition of [17]O-depleted barite at the aftermath of Nantuo glacial meltdown in South China. *Geology*, *38*(10), 903–906. https://doi.org/10.1130/G31224.1